




The Variable Fast Soft X-Ray Wind in PG 1211+143

J. N. Reeves¹ , A. Lobban², and K. A. Pounds³¹Center for Space Science and Technology, University of Maryland Baltimore County, 1000 Hilltop Circle, Baltimore, MD 21250, USA; jreeves@umbc.edu²Astrophysics Group, School of Physical and Geographical Sciences, Keele University, Keele, Staffordshire, ST5 5BG, UK³Dept. of Physics and Astronomy, University of Leicester, University Road, Leicester LE1 7RH, UK

Received 2017 October 16; revised 2017 December 19; accepted 2018 January 11; published 2018 February 8

Abstract

The analysis of a series of seven observations of the nearby ($z = 0.0809$) QSO PG 1211+143, taken with the Reflection Grating Spectrometer (RGS) onboard *XMM-Newton* in 2014, are presented. The high-resolution soft X-ray spectrum, with a total exposure exceeding 600 ks, shows a series of blueshifted absorption lines from the He and H-like transitions of N, O, and Ne, as well as from L-shell Fe. The strongest absorption lines are all systematically blueshifted by $-0.06c$, originating in two absorption zones from low- and high-ionization gas. Both zones are variable on timescales of days, with the variations in absorber opacity effectively explained by either column density changes or the absorber ionization responding directly to the continuum flux. We find that the soft X-ray absorbers probably exist in a two-phase wind at a radial distance of $\sim 10^{17}$ – 10^{18} cm from the black hole with the lower-ionization gas as denser clumps embedded within a higher-ionization outflow. The overall mass outflow rate of the soft X-ray wind may be as high as $2M_{\odot} \text{ yr}^{-1}$, close to the Eddington rate for PG 1211+143 and similar to that previously deduced from the Fe K absorption.

Key words: accretion, accretion disks – black hole physics – galaxies: active – galaxies: individual (PG 1211+143)

1. Introduction

The X-ray spectra of active galactic nuclei (AGNs) are commonly observed to display evidence for significant columns of ionized circumnuclear material within the vicinity of the central black hole. In particular, high-resolution X-ray spectra acquired with *XMM-Newton* and *Chandra* have revealed the presence of narrow, blueshifted absorption lines indicative of outflowing material in our line of sight (e.g., Kaastra et al. 2000; Kaspi et al. 2002; Crenshaw et al. 2003; McKernan et al. 2007). With the absorbing material typically outflowing with velocities on the order of a few times -100 km s^{-1} to $\sim -1000 \text{ km s}^{-1}$, these so-called “warm absorbers” are observed to be present in at least 50% of AGNs (e.g., Reynolds & Fabian 1995; Blustin et al. 2005).

In addition to the warm absorbers, typically observed in the soft X-ray band, the discovery of blueshifted absorption features from much more highly ionized material has provided strong evidence for the existence of high-velocity outflows. With the signature primarily manifesting itself in absorption lines from K-shell transitions of He-/H-like Fe, the measured blueshifts imply outflow velocities on the order of $\sim -0.1c$ or higher (e.g., APM 08279+5255, Chartas et al. 2002; PG 1211+143, Pounds et al. 2003; PDS 456, Reeves et al. 2003). The high velocities and ionization of the material suggests that the high-velocity outflows originate much closer to the black hole than the slower, less-ionized warm absorbers. More recent systematic studies of archival *XMM-Newton* (Tombesi et al. 2010, 2011) and *Suzaku* (Gofford et al. 2013) data have shown that high-velocity disk winds may be a common feature of luminous AGNs. With the derived outflow rates calculated to be high (up to $\sim \text{few } M_{\odot} \text{ yr}^{-1}$) and therefore comparable with the measured accretion rates of AGNs, the outflows are estimated to carry kinetic power of as much as a few percent of the bolometric luminosity, L_{bol} . As such, fast outflows likely play an important role in coupling together black hole growth and the properties of the host galaxy (King 2003, 2010) and

offer a possible interpretation of the M – σ relation for galaxies (Ferrarese & Merritt 2000; Gebhardt 2000).

While the evidence for high-velocity outflows in the hard X-ray/Fe K band is now well established, there is a relative scarcity of detections to date in the soft X-ray band. Detecting lower-ionization, soft-band counterparts of high-velocity outflows is important, not only to fully establish the presence of high-velocity outflows in AGNs but also to probe all phases of the outflowing gas—i.e., across a wide range of ionization and column density.

In addition to the original discovery of the fast wind in PG 1211+143 (Pounds et al. 2003), evidence has emerged for the presence of a fast soft X-ray absorber in several other AGNs. Notably, in PDS 456, Reeves et al. (2003) first noted the presence of blueshifted absorption in the soft X-ray band through an *XMM-Newton* observation in 2001. Here a broad absorption trough was resolved in the Reflection Grating Spectrometer (RGS) spectrum originating from a blend of L-shell transitions from highly ionized Fe near $\sim 1 \text{ keV}$ with a measured outflow velocity of $\sim -50,000 \text{ km s}^{-1}$ (in addition to the now well-established high-velocity outflow detected in the Fe K band). These high-velocity, soft-band counterparts of the outflow have since been confirmed in a multi-epoch analysis of all of the *XMM-Newton* observations of PDS 456 (Reeves et al. 2016).

Further claims of detections of high-velocity outflows in the soft X-ray band include Ark 564 (Gupta et al. 2013), where $K\alpha$ transitions of O VII and O VI were detected in absorption with a measured blueshift corresponding to $v_{\text{out}} \sim -0.1c$, and Mrk 590 (Gupta et al. 2015), primarily through the detection of blueshifted absorption lines from O VIII, Ne IX, Si XIV, and Mg XII ranging in outflow velocity from $-0.07c$ to $-0.18c$. Both observations were performed with the gratings onboard *Chandra*.

More recently, multiple velocity components of a fast outflow were observed in the *XMM-Newton* RGS spectrum of the narrow-line Seyfert 1 galaxy IRAS 17020+4544

(Longinotti et al. 2015), covering a wide range of ionization and column density with outflow velocities in the range $-23,000$ to $-33,000$ km s $^{-1}$. A soft-band absorber with a velocity of $\sim -0.24c$ was also observed in IRAS 13224–3809 (Parker et al. 2017) through high-resolution RGS data with a corresponding highly ionized Fe K counterpart and a claim of a correlation between the observed properties of the outflow and the luminosity of the source (Pinto et al. 2017b). A wealth of absorption lines were also observed in the RGS spectrum of NGC 4051 with velocity components of up to $\sim -10,000$ km s $^{-1}$ (Pounds & Vaughan 2011), interpreted as a cooling shocked flow (Pounds & King 2013). Finally, in addition to such detections in AGNs, evidence for high-velocity outflows in the soft X-ray band has also been seen in ultraluminous X-ray sources (ULXs)—e.g., in NGC 1313 X-1 and NGC 5408 X-1 (Pinto et al. 2016, 2017a, 2017c), with measured outflow velocities of $\sim -0.2c$.

This paper focuses on PG 1211+143, which is a luminous narrow-line Seyfert galaxy/quasi-stellar object (QSO) at a distance of 331 Mpc ($z = 0.0809$; Marziani et al. 1996). It is bright in both the optical and X-ray bands with an X-ray luminosity of the order of $\sim 10^{44}$ erg s $^{-1}$. While being known for its variability and spectral complexity, PG 1211+143 is primarily known for being the “prototype” source for high-velocity outflows, as it offered the first detection of a mildly relativistic outflow in a non-broad-absorption-line (BAL) AGN (Pounds et al. 2003; Pounds & Page 2006), with a velocity of $v_{\text{out}} \sim -0.1c$.

The initial detection of the high-velocity outflow was based on the detection of blueshifted absorption in the hard X-ray/Fe K band from the original 60 ks *XMM-Newton* observations in 2001. In addition to the Fe K band absorption, Pounds et al. (2003) also claimed the detection of several blueshifted absorption lines in the RGS spectra originating from the He and H-like lines of C, N, O, and Ne. Although Kaspi & Behar (2006) claimed a much lower velocity, a more recent analysis combining multiple resonance lines confirmed the soft X-ray outflow velocity of $-0.07c$ (Pounds 2014a). Photoionized absorption and emission spectra from three *XMM-Newton* observations were then modeled over a broad spectral band to estimate the mass outflow rate and energetics of the flow, suggesting that the outflow was significant in terms of galactic feedback (Pounds & Reeves 2007, 2009; Pounds 2014b).

This paper marks the sixth in a series of papers on an extended ~ 630 ks *XMM-Newton* observation acquired in 2014. In Pounds et al. (2016a), an analysis of the hard X-ray spectrum revealed significant velocity structure in the highly ionized wind, with primary velocities of $v/c \sim -0.06$ and $v/c \sim -0.13c$. In Pounds et al. (2016b), we extended the analysis to the soft X-ray band through the high signal-to-noise RGS spectrum, detecting lower-ionization high-velocity counterparts of the outflow. Meanwhile, the multiwavelength variability with *XMM-Newton* and a long-term *Swift* monitoring campaign was analyzed in Lobban et al. (2016a), while the broadband *XMM-Newton* + *NuSTAR* spectrum was analyzed in Lobban et al. (2016b), showing that the high-velocity wind model extends well toward the broad 0.3–79 keV bandpass. Finally, in Lobban et al. (2018), we analyzed the short-term X-ray variability of the source through interband Fourier time lags.

In this paper, we revisit the mean RGS spectrum from the *XMM-Newton* long look, finding that the dominant soft X-ray

absorption arises from low- and high-ionization gas outflowing with a common velocity of $-0.06c$. We then focus on the short-term variability of the outflow in the soft X-ray band on a timescale of \sim days through the analysis of high signal-to-noise interorbit RGS spectra, finding substantial short-term variability in the ultrafast outflow in PG 1211+143.

2. Observations and Data Reduction

PG 1211+143 was observed by *XMM-Newton* (Jansen et al. 2001) on seven occasions in 2014. The observations took place over a roughly five-week period from 2014 Jun 02 to 2014 Jul 07. The duration of the seven observations totaled ~ 630 ks, with each observation having a typical duration of ~ 100 ks, apart from the fifth observation, which was ~ 55 ks. In this paper, we primarily focus on data acquired with the RGS (den Herder et al. 2001) onboard *XMM-Newton*. All data were processed using the *XMM-Newton* Scientific Analysis Software (SAS⁴) package (version 15.0).

The RGSPROC⁵ script as part of SAS was used to extract first-order dispersed spectra from each of the two RGS modules. Observations were screened for periods of high background by examining light curves from the CCD closest to the optical axis of the telescope, resulting in net exposures ranging from 56.8 ks (per RGS module) for the shortest observation to 102.8 ks. The net background-subtracted count rates range from 0.086 ± 0.001 to 0.181 ± 0.002 ct s $^{-1}$ for RGS 1 and 0.088 ± 0.001 to 0.182 ± 0.001 ct s $^{-1}$ for RGS 2. These translate into 0.4–2 keV fluxes of $3.40_{-0.12}^{+0.07} \times 10^{-12}$ to $6.90_{-0.13}^{+0.14} \times 10^{-12}$ and $3.40 \pm 0.08 \times 10^{-12}$ to $6.60 \pm 0.12 \times 10^{-12}$ erg cm $^{-2}$ s $^{-1}$ for the two detectors, respectively. In all seven observations, the background count rate was just a few percent of the source rate. The exception to this is the very long-wavelength part of the RGS spectrum above 30 Å, as well as the very short-wavelength band below ~ 7.5 Å in the observed frame, where the effective area drops rapidly. Thus, the subsequent spectral analysis is restricted to 7.5–30 Å in the observed frame. All count rates and observed fluxes are listed in Table 1.

The RGS 1 and RGS 2 spectra were found to be consistent in each of the seven observations, and the subsequent spectral parameters were found to be consistent from fitting RGS 1+2 separately. As such, combined RGS 1+2 spectra were produced using the RGSCOMBINE⁶ task within SAS. Finally, we also combined the spectra from all seven observations to produce a high signal-to-noise time-averaged “mean” RGS 1+2 spectrum, having weighted the response files by exposure time. This spectrum has a mean count rate of 0.136 ± 0.001 ct s $^{-1}$ and 0.4–2 keV flux of $5.07 \pm 0.01 \times 10^{-12}$ erg cm $^{-2}$ s $^{-1}$. All spectra were binned using the SAS task SPECGROUP⁷ in such a way as to not oversample the intrinsic energy resolution of the detector(s) by any factor greater than 3. This also ensured that there were >25 ct bin $^{-1}$, thus allowing the use of χ^2 minimization. Note that the combined spectrum yielded a total of 173,000 net counts, while for the individual sequences, this ranges from 18,000 (rev 2659) to 32,000 (rev 2666) counts, sufficient for the use of χ^2 statistics. Errors are quoted at 90% confidence for one parameter of interest ($\Delta\chi^2 = 2.7$). All subsequent fits

⁴ <http://xmm.esac.esa.int/sas/>

⁵ <http://xmm-tools.cosmos.esa.int/external/sas/current/doc/rgsproc/>

⁶ <http://xmm-tools.cosmos.esa.int/external/sas/current/doc/rgscombine/>

⁷ <https://xmm-tools.cosmos.esa.int/external/sas/current/doc/specgroup/>

Table 1
Observation Log of the Seven *XMM-Newton* RGS Observations of PG 1211+143 in 2014

| Start Date | Obs. ID | XMM Rev. | Instrument | Exposure ^a | Count Rate ^b | Mean Flux ^c |
|-------------|------------|----------|------------|-----------------------|-------------------------|--|
| 2014 Jun 02 | 0745110101 | REV 2652 | RGS 1 | 85.7 | 0.137 ± 0.001 | 5.41 ^{+0.10} _{-0.11} |
| | | | RGS 2 | 85.6 | 0.136 ± 0.001 | 5.36 ^{+0.12} _{-0.10} |
| 2014 Jun 15 | 0745110201 | REV 2659 | RGS 1 | 102.7 | 0.086 ± 0.001 | 3.46 ^{+0.07} _{-0.12} |
| | | | RGS 2 | 102.8 | 0.088 ± 0.001 | 3.40 ^{+0.08} _{-0.08} |
| 2014 Jun 19 | 0745110301 | REV 2661 | RGS 1 | 101.1 | 0.130 ± 0.001 | 5.00 ^{+0.11} _{-0.09} |
| | | | RGS 2 | 101.2 | 0.126 ± 0.001 | 4.68 ^{+0.07} _{-0.09} |
| 2014 Jun 23 | 0745110401 | REV 2663 | RGS 1 | 98.7 | 0.136 ± 0.001 | 5.29 ^{+0.09} _{-0.09} |
| | | | RGS 2 | 98.8 | 0.133 ± 0.001 | 4.84 ^{+0.07} _{-0.08} |
| 2014 Jun 25 | 0745110501 | REV 2664 | RGS 1 | 56.8 | 0.181 ± 0.002 | 6.90 ^{+0.14} _{-0.13} |
| | | | RGS 2 | 56.8 | 0.182 ± 0.001 | 6.60 ^{+0.12} _{-0.12} |
| 2014 Jun 29 | 0745110601 | REV 2666 | RGS 1 | 94.0 | 0.169 ± 0.001 | 6.46 ^{+0.14} _{-0.06} |
| | | | RGS 2 | 94.0 | 0.173 ± 0.001 | 6.27 ^{+0.10} _{-0.13} |
| 2014 Jul 07 | 0745110701 | REV 2670 | RGS 1 | 97.6 | 0.134 ± 0.001 | 5.24 ^{+0.11} _{-0.06} |
| | | | RGS 2 | 97.7 | 0.132 ± 0.001 | 4.85 ^{+0.07} _{-0.09} |
| mean | | | RGS 1+2 | 1274 | 0.136 ± 0.001 | 5.07 ^{+0.01} _{-0.01} |

Notes. Count rates and mean fluxes are given over the 0.4–2 keV band.

^a Net exposure time in units of ks.

^b Observed background-subtracted count rate in units of ct s⁻¹.

^c Observed mean flux in units of $\times 10^{-12}$ erg cm⁻² s⁻¹.

are performed using the XSPEC spectral fitting package (Arnaud 1996).

3. Mean Spectral Analysis

In Figure 1, we show the combined RGS 1+2 light curve of PG 1211+143 over the soft 0.4–2 keV band. The source is observed to be highly variable in the soft band, varying in count rate by up to a factor of ~ 3 from as low as ~ 0.15 ct s⁻¹ during REV 2659 to ~ 0.5 ct s⁻¹ in REV 2664. In Figure 2, the soft-band light curve is placed into the context of a longer ~ 2 month monitoring campaign that we obtained with *Swift* (Gehrels et al. 2004), where we have overlaid the observed 0.4–2 keV *XMM-Newton* EPIC-pn and *Swift* XRT count rates. The broadband *XMM-Newton* and *Swift* variability is described in Lobban et al. (2016a), and we return to the soft-band spectral variability of PG 1211+143 later in Section 4. Our initial aim is to build a template model based on the mean spectrum of PG 1211+143 from the 2014 RGS observations, which then can be applied to all seven sequences (listed in Table 1) to study the variability of the fast soft X-ray wind. We start by revisiting the spectral features in the mean spectrum and their common outflow velocity, subsequently building upon that to construct a best-fitting photoionization model.

Note that outflow velocities are given in the rest frame of PG 1211+143 at $z = 0.0809$, accounting for relativistic Doppler shifts, where negative values of v/c correspond to blueshifted velocities. In order to calculate the outflow velocity (v_{out}) of an absorption-line system in the rest frame of PG 1211+143, the following prescription is used:

$$\frac{v_{\text{out}}}{c} = \frac{(1 + z_{\text{obs}})^2 - (1 + z_{\text{QSO}})^2}{(1 + z_{\text{obs}})^2 + (1 + z_{\text{QSO}})^2}, \quad (1)$$

where z_{obs} is the redshift of an absorption system in the observed frame and z_{QSO} is the QSO redshift ($z = 0.0809$).

3.1. Soft X-Ray Absorption and Emission Lines from PG 1211+143

To investigate the mean soft X-ray spectrum, which was initially analyzed in Pounds et al. (2016b), we constructed a simple baseline continuum model that we applied to the RGS spectrum over the rest-frame range 7–27.5 Å (or 7.5–30 Å observed frame), which covers the highest signal-to-noise ratio portion of the spectrum. A two-component continuum model was adopted consisting of two power laws, one of which is steep ($\Gamma \sim 3$) to account for the prominent soft excess in PG 1211+143 and one of which is a harder component ($\Gamma = 1.6$ –1.7) that dominates the broadband spectrum above 1 keV (Lobban et al. 2016a). A neutral photoelectric absorber associated with our Galaxy was also included via the XSPEC TBABS model (Wilms et al. 2000) using the absorption cross-sections of Verner et al. (1996) and the abundances of Wilms et al. (2000). This was initially set to the expected column density of $N_{\text{H}} = 2.9 \times 10^{20}$ cm⁻² (Kalberla et al. 2005) but was subsequently allowed to vary to allow for any column density in excess of this value.

The data/model residuals to this baseline continuum are shown in Figure 3, where all the significant lines occur over the wavelength range from 7 to 27 Å in the quasar rest frame (or up to 30 Å in the observed frame). Several prominent narrow absorption lines are present in the soft X-ray spectrum, primarily arising from the resonance He and H-like lines of N, O, and Ne, as well as from L-shell Fe. In Table 2, we list the centroid rest wavelengths of the most prominent absorption lines observed in the spectrum (detected at a minimum 95% confidence level), along with their most likely atomic identification and corresponding laboratory frame wavelength.

In total, there are 14 narrow lines (plus one edge) in Table 2, which can be identified with absorption at a consistent velocity, with a mean velocity shift of $-0.061 \pm 0.001c$. However, two lines may have uncertain identifications. The absorption line near ~ 17.5 Å may be associated with either O VII $1s \rightarrow 3p$ at $-0.06c$ or a higher-velocity component of O VIII $1s \rightarrow 2p$ at

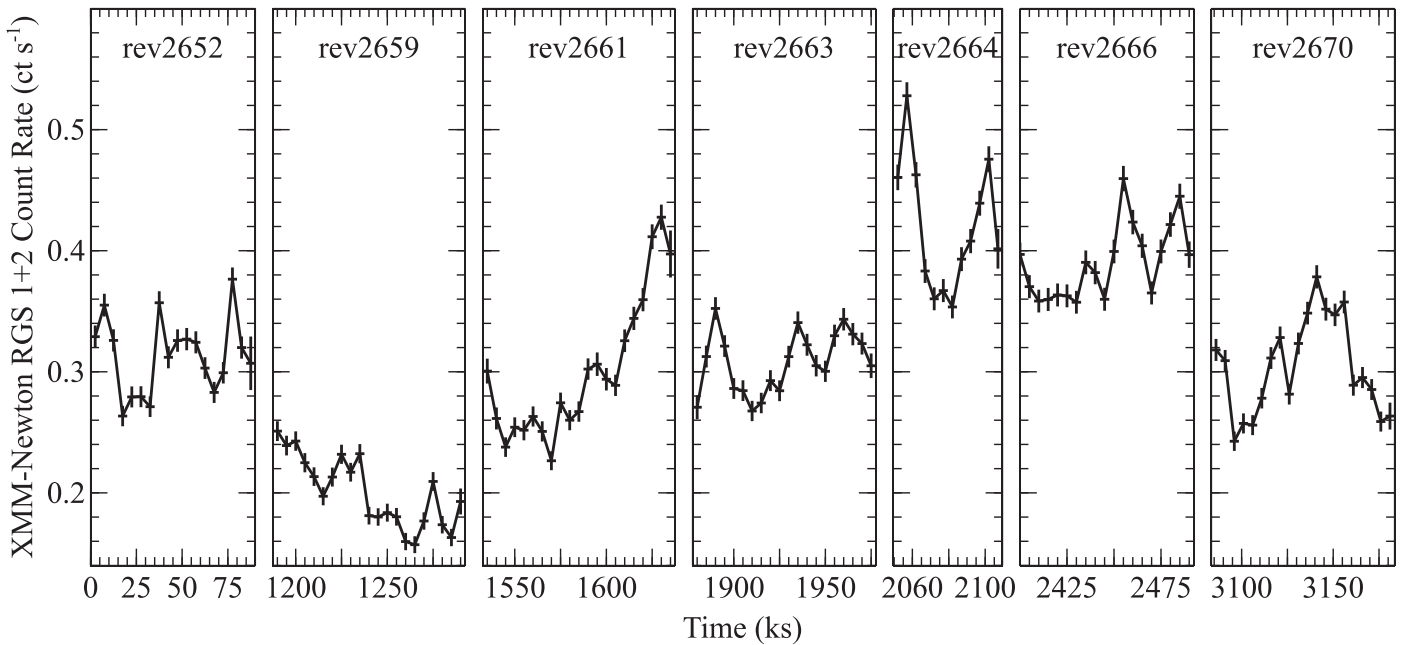


Figure 1. *XMM-Newton* first-order 0.4–2 keV RGS 1+2 light curve of PG 1211+143 in 5 ks time bins. The light curve shows the relative variability between all seven *XMM-Newton* sequences in the soft band, with REV 2659 the lowest-flux observation. Note the gaps between the observations, where the x -axis corresponds to time since the beginning of the campaign in REV 2652. See Table 1 for the details of the individual *XMM-Newton* sequences.

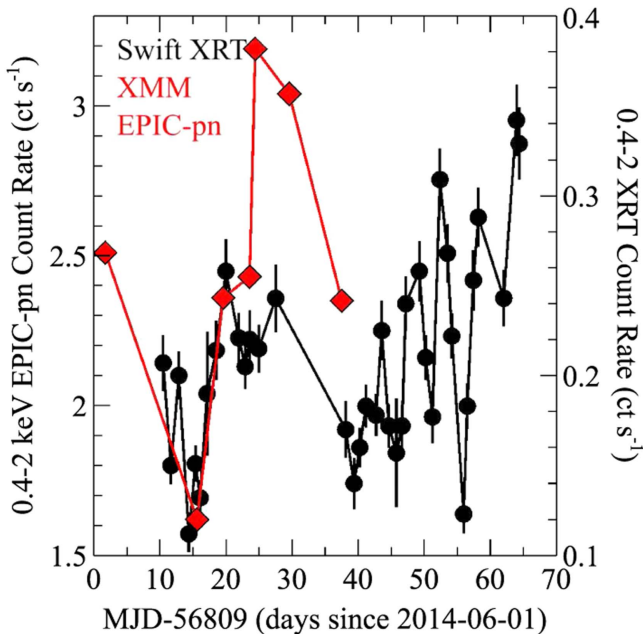


Figure 2. Overlaid *XMM-Newton* EPIC-pn (red diamonds) and *Swift* XRT (black circles) light curve in the 0.4–2 keV band showing the long-term soft X-ray variability of PG 1211+143. Note that the second *XMM-Newton* point in REV 2659 occurs during a period of low soft X-ray flux ~ 15 days after the start of the observational campaign. The soft X-ray flux then increases, peaking in *XMM-Newton* REV 2664.

$-0.08c$. In addition, the absorption line at 12.4 \AA could also be associated with a higher- ($-0.08c$) velocity component of Ne IX $1s \rightarrow 2p$, with no obvious lower-velocity counterpart. This supports the earlier Gaussian analysis presented in Pounds et al. (2016b) confirming the presence of a soft X-ray counterpart to the wind, which was originally claimed in Pounds et al. (2003) on the basis of the initial 60 ks *XMM-Newton* observation in 2001.

In addition to the narrow blueshifted absorption lines, a broad absorption trough is also clearly present, centered at $\sim 15.3 \text{ \AA}$ in the quasar rest frame (Figure 3; upper panel). This is most likely associated with the Fe M-shell unresolved transition array (UTA), which originates from a blend of $2p \rightarrow 3d$ transitions from low-ionization Fe (Fe I–XVII; Behar et al. 2001). This broad feature has been observed in the warm absorbers in many Type I AGNs; e.g., IRAS 13349+2438 (Sako et al. 2001), NGC 3783 (Kaspi et al. 2002; Krongold et al. 2003), NGC 5548 (Kaastra et al. 2002), Mrk 509 (Pounds et al. 2001; Detmers 2011), NGC 7469 (Blustin et al. 2007), Mrk 841 (Longinotti et al. 2010), IC 4239A (Steenbrugge et al. 2005), NGC 3516 (Holczer & Behar 2012), MCG-6-30-15 (Lee et al. 2001; Turner et al. 2004), NGC 4051 (Pounds et al. 2004), and Mrk 279 (Costantini et al. 2007). It typically occurs between 16 and 17 \AA , depending on the exact ionization of the absorber.

In Figure 4, we compare the spectrum of PG 1211+143 with another nearby QSO of similar luminosity, MR 2251-178 (at $z = 0.064$), which is well known for its soft X-ray warm absorber (e.g., Halpern 1984; Kaspi et al. 2004; Reeves et al. 2013). The RGS data for the latter were taken from a long ~ 300 ks *XMM-Newton* RGS observation in 2011, presented in Reeves et al. (2013). In MR 2251-178, the absorber outflow velocity is low ($< 1000 \text{ km s}^{-1}$), providing an interesting contrast to PG 1211+143.

The rest-frame comparison between the two spectra clearly shows that the broad UTA is present toward both quasars, but it is blueshifted in PG 1211+143 (centered at 15.3 \AA) compared to what is measured in MR 2251-178 (where the UTA is centered close to 16.5 \AA). While some variation in the UTA position can be caused by variable ionization due to the relative contribution of the different Fe ions toward the UTA (Behar et al. 2001), as we will show later in Section 3.2, the relative blueshift of the UTA in PG 1211+143 is consistent with an outflow velocity of $-0.06c$. In addition, it is also apparent

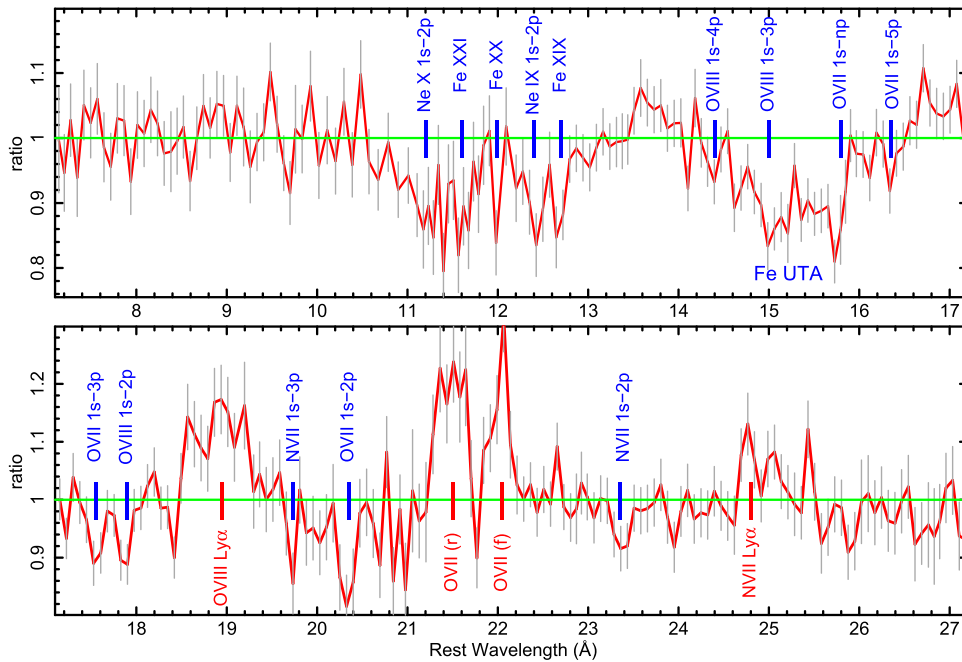


Figure 3. Mean *XMM-Newton* RGS 1+2 spectrum of PG 1211+143 with a total exposure of ~ 640 ks plotted as a ratio to the baseline double power-law continuum model. The data are binned by a factor of $\times 2$ for clarity. The upper panel shows the 7–17 Å band and the lower panel 17–27 Å in the quasar rest frame at $z = 0.0809$. Data are shown as red histograms, while 1σ error bars are in gray. Several strong resonance ($1s \rightarrow 2p$) absorption lines from Ne, O, N, and L-shell Fe are present in the spectrum. These are systematically blueshifted with respect to their known wavelengths by an outflow velocity of -0.06 up to $-0.08c$ (see Table 2). The broad absorption trough at ~ 15 Å is due to a blueshifted Fe M-shell UTA. Note also the presence of strong and broadened emission lines, especially due to the O VII triplet (21.6–22.1 Å) and O VIII Ly α (19 Å).

Table 2
Blueshifted Absorption Lines Identified in the Mean
2014 RGS Spectrum of PG 1211+143

| Rest λ (Å) ^a | Line ID ^b | Lab λ (Å) ^b | v/c ^c |
|---------------------------------|-------------------------------|--------------------------------|----------------------|
| 23.35 | N VII $1s \rightarrow 2p$ | 24.78 | -0.059 ± 0.002 |
| 20.33 | O VII $1s \rightarrow 2p$ | 21.60 | -0.060 ± 0.002 |
| 19.71 | N VII $1s \rightarrow 3p$ | 20.91 | -0.059 ± 0.002 |
| 17.86 | O VIII $1s \rightarrow 2p$ | 18.97 | -0.060 ± 0.002 |
| 17.54 | O VII $1s \rightarrow 3p$ | 18.63 | -0.060 ± 0.002 |
| ... | or O VIII $1s \rightarrow 2p$ | 18.97 | $-0.078 \pm 0.002^*$ |
| 16.32 | O VII $1s \rightarrow 5p$ | 17.40 | -0.064 ± 0.002 |
| 16.10 | O VII $1s \rightarrow 6p$ | 17.20 | -0.066 ± 0.002 |
| 15.80 | O VII edge | 16.77 | -0.059 ± 0.002 |
| 14.99 | O VIII $1s \rightarrow 3p$ | 16.00 | -0.065 ± 0.003 |
| 14.29 | O VIII $1s \rightarrow 4p$ | 15.18 | -0.060 ± 0.003 |
| 12.65 | Ne IX $1s \rightarrow 2p$ | 13.45 | -0.061 ± 0.003 |
| ... | or Fe XIX $2p \rightarrow 3d$ | 13.52 | -0.064 ± 0.004 |
| 12.41 | Ne IX $1s \rightarrow 2p$ | 13.45 | $-0.080 \pm 0.003^*$ |
| 11.99 | Fe XX $2p \rightarrow 3d$ | 12.82 | -0.066 ± 0.004 |
| 11.55 | Fe XXI $2p \rightarrow 3d$ | 12.28 | -0.061 ± 0.004 |
| 11.35 | Ne X $1s \rightarrow 2p$ | 12.14 | -0.067 ± 0.004 |

Notes. *Denotes a possible higher-velocity component.

^a Centroid rest wavelength of an absorption line in Å, with a typical uncertainty of $\Delta\lambda = 0.04$ Å.

^b Probable line ID and known laboratory wavelength from <http://www.nist.gov>.

^c Derived blueshift of absorption line in units of c . The majority of lines are systematically blueshifted with a mean velocity of $-0.062 \pm 0.001c$.

when compared to MR 2251-178 that the principal narrow absorption lines are systematically blueshifted in PG 1211+143. For instance, the Ne IX and Ne X $1s \rightarrow 2p$ resonance

absorption lines are detected very close to their expected rest wavelengths in MR 2251-178 (at 13.4 and 12.1 Å, respectively) with little blueshift, while in PG 1211+143, these lines are strongly blueshifted (12.4 and 11.3 Å, respectively). A similar case is seen for the O VIII Ly α line, which is observed very close to its known wavelength near ~ 19 Å in MR 2251-178 but is blueshifted (at 17.9 Å) in PG 1211+143 with respect to the strong emission line that is observed at 19 Å. Likewise, the O VII $1s \rightarrow 2p$ absorption line (at 20.3 Å) is blueshifted with respect to the corresponding resonance emission line in MR 2251-178 at 21.6 Å.

Strong emission lines are also seen in PG 1211+143 and are apparent in Figures 3 and 4, particularly from O VII and O VIII. The parameters of the significant emission lines fitted with Gaussian profiles are listed in Table 3. Most notable is the O VII triplet, which is resolved into a forbidden component (at 22.1 Å) and a resonance line (21.46 ± 0.06 Å), the latter of which is mildly blueshifted with respect to its expected rest wavelength (at 21.60 Å). Generally, the emission-line profiles are all significantly broadened with respect to the RGS resolution, the exception being the O VII forbidden line, which is relatively narrow (FWHM ~ 1200 km s $^{-1}$). For the other emission lines, the typical FWHM velocity widths are in the range of ~ 5000 – $10,000$ km s $^{-1}$; indeed, one of the strongest emission lines is from O VIII Ly α at 19 Å, which has a FWHM of $\sim 11,000$ km s $^{-1}$ (see Table 3). These widths are much broader than the typical optical permitted emission lines seen from PG 1211+143, where the H β width is relatively narrow with a FWHM of 1860 km s $^{-1}$ (Boroson & Green 1992). This suggests that the soft X-ray line emission could be associated with gas coincident with an innermost X-ray component of the broad-line region (BLR) or that it arises from reemission

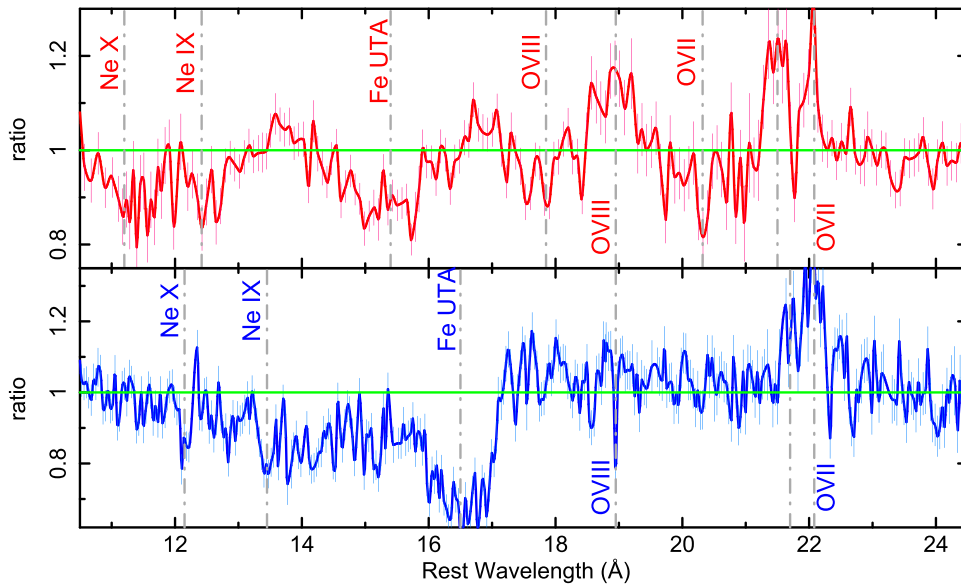


Figure 4. Comparison between the mean RGS spectrum of PG 1211+143 (upper panel, red points) and that of the nearby ($z = 0.064$) radio-quiet QSO MR 2251-178 (lower panel, blue points) plotted over the 10–25 Å range. MR 2251-178 exhibits a classic slow warm absorber with little or no blueshift (see Reeves et al. 2013), where the strongest absorption/emission features are marked with dashed lines in their rest-frame wavelength. In contrast, the strong absorption features from PG 1211+143—for instance, from O VII, O VIII, Ne IX, Ne X, and the Fe M-shell UTA—are all systematically blueshifted compared to MR 2251-178.

associated with a wide-angle wind. We discuss the latter possibility further later (see Section 3.4).

We also fitted some of the absorption lines with Gaussian profiles using the $1s \rightarrow 2p$ lines from N VII, O VII, and O VIII, which are relatively isolated line profiles. For these three lines, we obtain a mean Gaussian width of $\sigma = 800^{+350}_{-240}$ km s $^{-1}$ (or FWHM ~ 1800 km s $^{-1}$). In contrast, the 1σ velocity resolution of the RGS is $\sigma \sim 400$ km s $^{-1}$ at the position of the O VII absorption line. Thus, unlike for the emission lines, the absorption lines appear to be marginally resolved compared to the instrumental resolution.

3.2. Photoionization Modeling

Next, we constructed a photoionized absorption model to account for the mean 2014 RGS spectrum of PG 1211+143. The continuum form with two power laws described above was adopted. The phenomenological form of the model is $\text{TBABS} \times [\text{XSTAR}_{\text{ABS}} \times (\text{POW}_{\text{HARD}} + \text{BBODY}) + \text{POW}_{\text{SOFT}} + \text{XSTAR}_{\text{EMISSION}}]$.

Here $\text{XSTAR}_{\text{ABS}}$ represents the multiplicative photoionized absorption grids of models generated by XSTAR (Kallman et al. 1996) that are applied to the continuum, while $\text{XSTAR}_{\text{EMISSION}}$ represents the additive photoionized emission tables generated by XSTAR in order to self-consistently fit the line emission (see below). Only one of the power-law continuum components (POW_{HARD}) is absorbed by the photoionized absorbers, while the other power law (POW_{SOFT}) emerges unattenuated by the photoionized absorbers. The neutral Galactic absorption component (TBABS) absorbs all of the emission components. The BBODY component is initially included to account for any additional soft excess that may be required, as may originate from the high-energy Wien tail of any disk emission. However, such a component was not required over the wavelength range analyzed in the RGS spectra (up to 30 Å observed frame) and thus was subsequently omitted from the analysis.

The XSTAR grids of models are identical to the ones that we generated in a previous analysis of PG 1211+143 (e.g., Pounds et al. 2016a, 2016b). These were calculated with the spectral energy distribution (SED) derived for PG 1211+143 from the simultaneous *XMM-Newton* optical monitor photometry and the mean 2014 EPIC-pn spectrum, which was parameterized by a double broken power-law model; see Lobban et al. (2016a) for details. The total 1–1000 Ryd ionizing luminosity from this SED was found to be 4×10^{45} erg s $^{-1}$, which was input into the XSTAR models.

Both multiplicative absorption tables, as well as additive emission tables (in the forward direction), were generated to account for both the ionized absorption and emission lines observed in the soft X-ray spectrum. Grids were run for three different turbulence velocities,⁸ with $b = 300$, 1000, and 3000 km s $^{-1}$. Note that the lower two turbulences correspond to velocity widths that well match the relatively narrow absorption lines, where the mean Gaussian width is $\sigma = 800^{+350}_{-240}$ km s $^{-1}$ (or FWHM ~ 1800 km s $^{-1}$), and give statistically equivalent fits. The broader $b = 3000$ km s $^{-1}$ grids were used to fit the photoionized emission, as the emission lines appear substantially broadened, as described in Section 3.1. Each grid was also generated with three different Fe abundances relative to the solar values of Grevesse & Sauval (1998), consisting of $\times 1$, $\times 3$, and $\times 5$ solar for Fe. As discussed in Pounds et al. (2016b), a higher abundance of Fe is driven by the requirement to fit the strong UTA absorption. Indeed, a worse fit was obtained using a solar abundance of Fe, whereas statistically equivalent fits were obtained for $\times 3$ and $\times 5$ abundances of Fe; thus, grids with $\times 3$ Fe abundance were subsequently adopted in all of the fits.

Prior to modeling the photoionized emission and absorption, the overall fit statistic to the baseline double power-law continuum model is extremely poor, with a reduced χ^2 of $\chi^2_{\nu} = 956.3/595 = 1.61$ and a corresponding null hypothesis probability for the model to be acceptable of $p = 2.7 \times 10^{-19}$.

⁸ The turbulence velocity width is defined as $b = \sqrt{2}\sigma = \text{FWHM}/(2\sqrt{\ln 2})$.

Table 3
Soft X-Ray Emission Lines in the PG 1211+143 RGS Spectrum

| Line ID | $\lambda_{\text{quasar}}^a$ | Flux ^b | EW ^c | σ_v^d | FWHM ^e | $\Delta\chi^2_f$ |
|-------------------------|--|----------------------|----------------------|-------------------------|--------------------------|------------------|
| N VII Ly α | 24.98 \pm 0.16 (496.2 $^{+3.2}_{-3.2}$) | 2.7 $^{+1.6}_{-1.2}$ | 1.0 $^{+0.6}_{-0.4}$ | 3100 $^{+1800}_{-1500}$ | 7300 $^{+4200}_{-3500}$ | 14.8 |
| O VII (f) | 22.07 \pm 0.03 (561.8 $^{+0.8}_{-0.6}$) | 2.4 $^{+0.8}_{-0.6}$ | 1.4 $^{+0.5}_{-0.4}$ | 530 $^{+500}_{-270}$ | 1240 $^{+1200}_{-630}$ | 26.5 |
| O VII (r) | 21.46 \pm 0.11 (577.8 $^{+3.2}_{-3.0}$) | 2.4 $^{+1.0}_{-1.0}$ | 1.5 $^{+0.6}_{-0.6}$ | 2230 $^{+1300}_{-780}$ | 5250 $^{+3050}_{-1830}$ | 15.4 |
| O VIII Ly α | 18.96 \pm 0.08 (653.9 $^{+2.9}_{-2.9}$) | 5.0 $^{+1.2}_{-1.0}$ | 4.9 $^{+1.2}_{-1.0}$ | 4700 $^{+1400}_{-960}$ | 11100 $^{+3700}_{-2300}$ | 63.2 |
| O VIII RRC ^g | 16.84 \pm 0.09 (736.0 $^{+4.0}_{-4.0}$) | 1.9 $^{+0.6}_{-0.5}$ | 2.8 $^{+0.9}_{-0.7}$ | ... | ... | 39.1 |
| Ne IX ^h (f) | 13.68 \pm 0.11 (906.0 $^{+7.0}_{-7.0}$) | 1.0 $^{+0.3}_{-0.3}$ | 2.7 $^{+1.0}_{-1.0}$ | 4000 $^{+2000}_{-1700}$ | 9400 $^{+4600}_{-4000}$ | 21.3 |

Notes.

^a Rest wavelength in units of \AA in quasar rest frame. Rest energy in eV given in parentheses.

^b Photon flux in units of $\times 10^{-5}$ photons cm^{-2} s^{-1} .

^c Equivalent width in quasar rest frame in units of eV.

^d 1σ velocity width in units of km s^{-1} .

^e FWHM velocity width in units of km s^{-1} .

^f Improvement in $\Delta\chi^2$ upon adding line to model.

^g Temperature of RRC constrained to $kT = 18^{+14}_{-6}$ eV.

^h Note that the broad Ne IX line may also be blended with a contribution from an O VIII RRC.

Table 4
Properties of the Photoionized Absorber/Emission Components Fitted to the Mean RGS Spectrum

| Parameters | Zone 1a | Zone 1b | Zone 2 | Zone 3 |
|--|-------------------------|-------------------------|-------------------------|-------------------------|
| Absorption: | | | | |
| N_{H} ($\times 10^{21}$ cm^{-2}) | 1.40 $^{+0.42}_{-0.36}$ | 10.0 $^{+6.0}_{-4.8}$ | 0.89 $^{+0.35}_{-0.27}$ | 1.6 $^{+0.8}_{-0.6}$ |
| $\log \xi$ | 1.32 $^{+0.15}_{-0.20}$ | 3.37 $^{+0.08}_{-0.12}$ | 2.03 $^{+0.17}_{-0.11}$ | 2.51 $^{+0.12}_{-0.20}$ |
| v/c | -0.062 \pm 0.001 | -0.059 \pm 0.002 | -0.077 \pm 0.001 | -0.187 \pm 0.002 |
| $\Delta\chi^2_{2\sigma}$ | 121.9 | 28.3 | 21.1 | 18.5 |
| P_{N}^b | 5.1×10^{-25} | 2.2×10^{-5} | 5.4×10^{-4} | 9.6×10^{-4} |
| Emission: | | | | |
| N_{H} ($\times 10^{21}$ cm^{-2}) | 1.4 ^t | 10 ^t | | |
| $\log \xi$ | 2.0 $^{+0.4}_{-0.3}$ | 3.4 ^t | | |
| v/c | <0.002 | -0.017 \pm 0.006 | | |
| κ_{xstar}^c | 0.70 \pm 0.25 | 1.7 \pm 0.7 | | |
| $f_{\text{cov}} = \Omega/4\pi^d$ | 0.20 \pm 0.06 | 0.46 \pm 0.20 | | |
| $\Delta\chi^2_{2\sigma}$ | 52.4 | 21.7 | | |
| P_{N}^b | 2.4×10^{-9} | 3.1×10^{-4} | | |

Notes.

^a Improvement in fit statistic from adding the absorption or emission zone to the model.

^b Null probability of adding the XSTAR zone, calculated via an F -test.

^c Measured normalization of XSTAR emission component, where $\kappa_{\text{xstar}} = f_{\text{cov}} L_{38}/D_{\text{kpc}}^2$, where f_{cov} is the covering fraction ($f = \Omega/4\pi$), L_{38} is the 1–1000 Ryd ionizing luminosity in units of 10^{38} erg s^{-1} , and D_{kpc} is the distance to PG 1211+143 in units of kpc.

^d Global covering fraction of the XSTAR emission component derived from the measured normalization of the emitter. See the text for details.

^t Denotes parameter is tied.

Thus, such a simple model, with no ionized emission or absorption, is rejected by the data at a high level of significance, which is apparent from the data/model residuals present in Figure 3.

3.3. Absorption Components

In order to obtain an acceptable fit to the ionized absorption present in the spectrum, successive absorption zones were then applied to the spectrum until the addition of further absorption grids no longer improved the fit at the 99% confidence level. Emission was also included by additive photoionized emission grids and is described further below (Section 3.4). The parameters of the absorption zones are summarized in Table 4, while the overall best fit to the XSTAR model is plotted in Figure 5. Here

four absorbers (zones 1a, 1b, 2, and 3) were required at >99.99% confidence, and these are described further below.

As noted earlier from the Gaussian line analysis, most of the absorption is associated with gas outflowing with $v/c = -0.06$, which is parameterized by zones 1a and 1b. Adding these zones of absorption against the baseline continuum leads to corresponding improvements in the fit statistic of $\Delta\chi^2 = 121.9$ and $\Delta\chi^2 = 28.3$, respectively. The relative contributions of these two absorption zones are also shown in Figure 6. Zone 1a is a lower-ionization zone, with $N_{\text{H}} = 1.4 \pm 0.4 \times 10^{21}$ cm^{-2} , an ionization parameter⁹ of

⁹ The ionization parameter is defined as $\xi = L_{\text{ion}}/nR^2$ (Tarter et al. 1969), where L_{ion} is the 1–1000 Ryd ionizing luminosity, n is the electron density, and R is the distance of the ionizing source from the absorbing clouds. The units of ξ are erg cm s^{-1} .

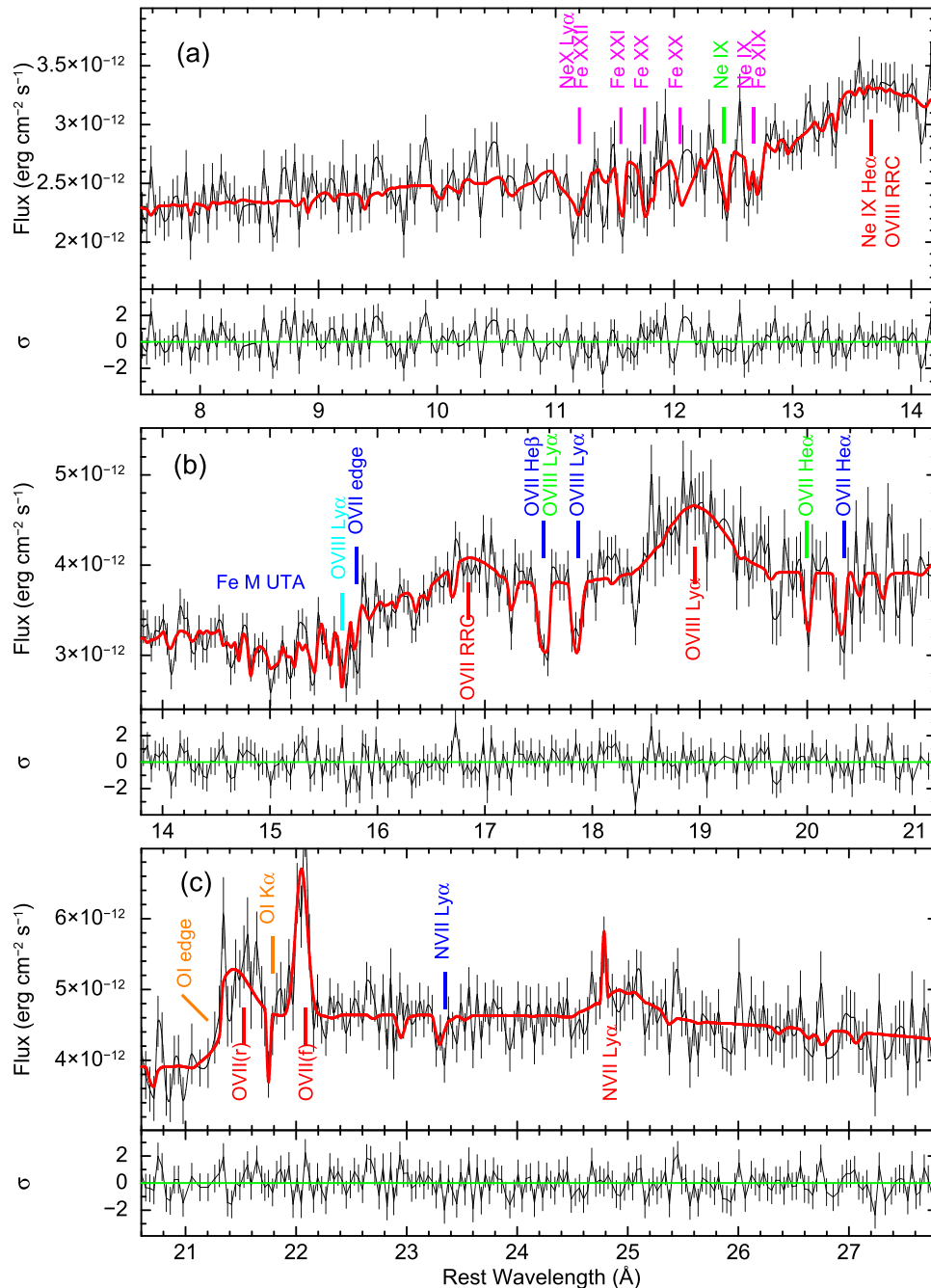


Figure 5. Best-fitting XSTAR model (red line) fitted to the mean RGS spectrum of PG 1211+143. Panel (a) shows the iron L-shell band, panel (b) shows the O VII–VIII and Fe M-shell band, and panel (c) shows the O VII triplet and N K-shell band. The spectrum is fitted down to 27.8 Å in the quasar rest frame (30 Å in the observed frame). The strongest atomic features are marked on the panels and color-coded to represent the different absorption and emission zones listed in Table 4. The blue labels correspond to absorber zone 1a (low ionization; Fe M-shell UTA and He/H-like N/O) and the magenta labels to zone 1b (high ionization; Fe L-shell and He/H-like Ne), both at an outflow velocity of $-0.06c$. The green labels correspond to zone 2 with an outflow velocity of $-0.08c$ (seen from O VII, O VIII, and Ne IX), and the cyan label corresponds to zone 3 ($-0.18c$), although the latter ID is uncertain. The red labels correspond to the broadened emission lines present in the spectrum, which, in particular, include the forbidden and resonance components of O VII and associated RRC emission at ~ 17 Å, as well as a strong, broad (FWHM $\sim 10,000$ km s^{-1}) emission line from O VIII Ly α . The orange labels mark the O I features produced by the Galactic ($z = 0$) neutral absorber. Overall, the model reproduces the observed features in the spectrum, and most of the remaining residuals agree within $\pm 2\sigma$.

$\log \xi = 1.32^{+0.15}_{-0.20}$, and an outflow velocity of $v/c = -0.062 \pm 0.001$. It is the most significant zone, carrying most of the absorber opacity, including the Fe M-shell UTA and the He/H-like lines of N and O, the former of which also appears to be associated with gas at a velocity of $\sim -0.06c$ rather than a slow warm-absorber component. Indeed, these features (marked by blue labels) are well modeled in the best-fit

spectrum shown in Figure 5, including the broad Fe M-shell UTA at around 15 Å and the $1s \rightarrow 2p$ resonance lines from O VIII (17.9 Å), O VII (20.4 Å), and N VII (23.3 Å).

Zone 1b represents the high-ionization phase of the $\sim -0.06c$ outflow, with a column density of $N_H = 1.0^{+0.6}_{-0.4} \times 10^{22}$ cm $^{-2}$, an ionization of $\log \xi = 3.4 \pm 0.1$, and a similar outflow velocity of $v/c = -0.059 \pm 0.002$. This zone contributes

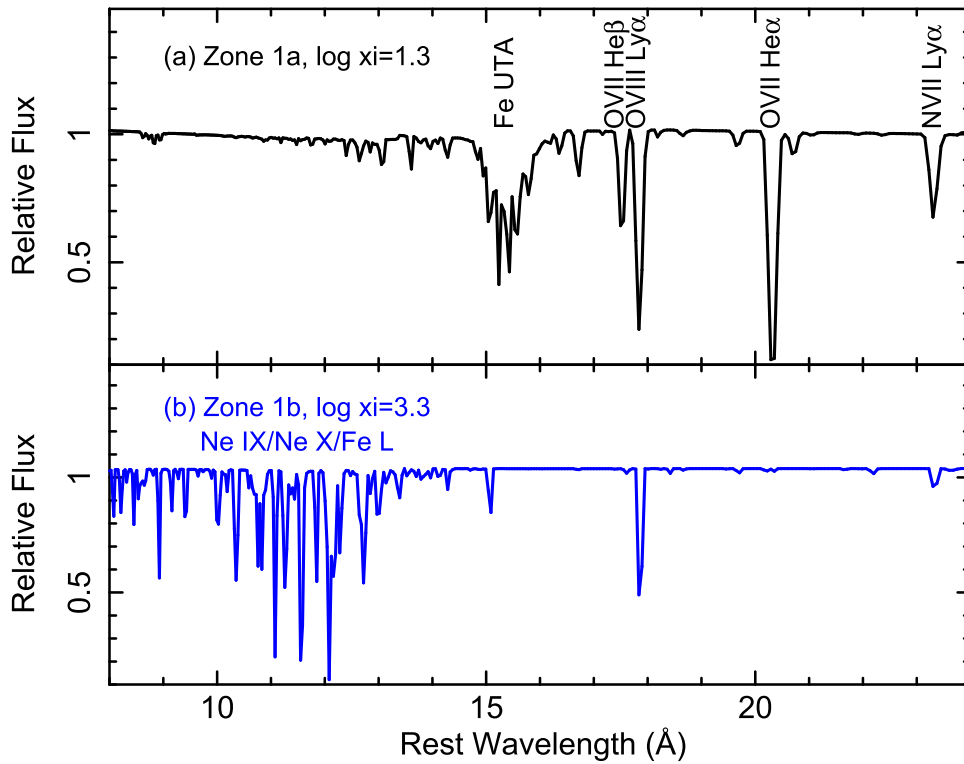


Figure 6. Relative transmission through the two main ionization zones of the absorbers. The upper panel shows the low-ionization zone 1a ($\log \xi = 1.3$), and the lower panel shows the high-ionization zone 1b ($\log \xi = 3.3$). Both zones are outflowing with $v/c = -0.06$ (see Table 4 for details). The lower-ionization zone 1a reproduces the strong blueshifted Fe M-shell UTA, as well as the He/H-like lines of N and O. The high-ionization zone 1b reproduces the strong series of Fe L-shell lines between 10 and 12 Å, as well as absorption from Ne IX–X and O VIII.

toward the blend of absorption between ~ 11 and 13 Å (Figure 5, panel (a), magenta labels) due to higher-ionization L-shell Fe (Fe XIX–XXII $2p \rightarrow 3d$). This zone also contributes to absorption from the $1s \rightarrow 2p$ transitions from Ne IX (12.6 Å) and Ne X (11.2 Å), as well as the O VIII Ly α absorption line at 17.9 Å.

The addition of these two $-0.06c$ zones largely accounts for most of the ionized absorption present in the spectrum shown in Figure 5. Nonetheless, there is some evidence for two possible higher-velocity zones. Zone 2 is associated with gas with an outflow velocity of $v/c = -0.077 \pm 0.001$, a column density of $N_{\text{H}} = 0.9 \pm 0.3 \times 10^{21} \text{ cm}^{-2}$, and an ionization of $\log \xi = 2.03^{+0.17}_{-0.11}$; its addition to the model led to a fit improvement of $\Delta\chi^2 = 21.1$. Its contribution toward the spectrum is more subtle, effectively adding a higher-velocity component blueward of the O VII and O VIII $1s \rightarrow 2p$ line profiles near ~ 20.0 and ~ 17.6 Å, respectively (see Figure 5; green labels). Note that the latter line may also be, in part, associated with O VII He β ($1s \rightarrow 3p$) at $-0.06c$, as was discussed above (Section 3.1) in the Gaussian line analysis. Zone 2 may also contribute to a $-0.08c$ component of Ne IX at 12.4 Å (Figure 5, panel (a)).

A third high-velocity component (zone 3), with $v/c = -0.187 \pm 0.002$, is formally required ($\Delta\chi^2 = 18.5$) and was noted by Pounds et al. (2016b), in addition to the above slower zones, in an earlier analysis of the mean spectrum. However, unlike for the $-0.06c$ and $-0.08c$ zones, the association of this absorption zone with discrete lines in the RGS spectrum is not easily apparent. Its main effect is to produce an absorption dip around 15.7 Å near the UTA due to blueshifted O VIII Ly α (see

Figure 5, panel (b), cyan label); thus, given its uncertain identification, this additional fast zone is not considered further.

In addition to the above outflowing absorption zones, a neutral absorption component is required associated with our Galaxy at $z = 0$. The best-fit column density is $N_{\text{H}} = 6.5^{+1.0}_{-1.2} \times 10^{20} \text{ cm}^{-2}$ and is about twice that predicted from the 21 cm value of $N_{\text{H}} = 2.9 \times 10^{20} \text{ cm}^{-2}$. The excess column density may be due to molecular hydrogen along the line of sight in our Galaxy, which would otherwise be missed in 21 cm surveys but would still be detected in the X-ray spectrum (Willingale et al. 2013). Note that we also cannot rule out some contribution from neutral gas associated with the host galaxy of PG 1211+143. The neutral absorber contributes to the O I edge, observed at $z = 0$ near 23.0 Å (or 21.4 Å in the QSO frame), as well as a weak O I K α absorption line observed at 23.5 Å (or 21.75 Å in the QSO frame). These neutral absorption features are apparent in Figure 5, as marked by the orange labels in panel (c) in the O K-shell band.

Note that the best-fit absorption model (together with emission lines as modeled below) produces a final acceptable fit of $\chi^2_{\nu} = 631.5/573 = 1.10$, while generally there are no other clear systematic residuals within the $\pm 2\sigma$ level present against the best fit shown in Figure 5. The only remaining residual at $>2\sigma$ against the best fit model lies at 18.4 Å, just blueward of the O VIII Ly α emission line (Figure 5, panel (b)). If this absorption feature is associated with O VIII Ly α , then its outflow velocity is $-0.03c$, which is intermediate between the above fast outflow zones and a slower warm absorber. However, no such velocity component appears to be associated with any of the other ions, and we note that one would typically

expect to observe one to two features purely by statistical chance at the 3σ level over a 600 channel spectrum.

As a final consistency check, we also tested a solar abundance absorber by replacing the $\times 3$ Fe abundance grid with the respective solar one for all of the zones. The overall fit statistic is acceptable, $\chi^2_\nu = 650.7/573$, although it is still formally worse than the $\times 3$ solar case (by $\Delta\chi^2 = 19.2$). The differences in the fits are subtle, but the main difference arises from the O features being slightly overpredicted with respect to the UTA, with the high-ionization iron L-shell features being somewhat underpredicted. However, overall, the fit parameters are all consistent with those listed in Table 4, with the only significant change being an increase in the column of the low-ionization zone 1a from $N_{\text{H}} = 1.4 \pm 0.4 \times 10^{21}$ to $N_{\text{H}} = 2.5 \pm 0.6 \times 10^{21} \text{ cm}^{-2}$ in order to reproduce the depth of the UTA.

3.3.1. The Lack of a Warm Absorber

Importantly, there do not appear to be any absorption features with zero (or low) velocity shift in the spectrum, which could be associated with a low-velocity warm absorber that is more commonly observed in Seyfert 1 galaxies. For instance, from inspecting Figure 5, there appear to be no absorption residuals at wavelengths close to the expected transitions of N VII Ly α (at 24.78 Å), O VII $1s \rightarrow 2p$ (21.60 Å), O VIII Ly α (18.97 Å), or Ne IX $1s \rightarrow 2p$ (13.45 Å), all of which are frequently detected in warm-absorber spectra. Indeed, the absorption features that are observed are strongly blueshifted with respect to their corresponding emission features, e.g., O VII He α or O VIII Ly α .

Nonetheless, we place upper limits on the presence of a warm absorber in the PG 1211+143 spectrum. We test the presence of a warm absorber from adopting the same XSTAR absorption grid but restricting the outflow velocity to within $\pm 0.01c$ of the systemic velocity of PG 1211+143. In this case, over three different ionization regimes, we find upper limits of $N_{\text{H}} < 2.5 \times 10^{19}$, $N_{\text{H}} < 4.0 \times 10^{19}$, and $N_{\text{H}} < 1.8 \times 10^{20} \text{ cm}^{-2}$ for $\log \xi = 1, 2, \text{ and } 3$, respectively. These limits are more than an order of magnitude lower than the respective ionization zones for the fast absorber, ruling out the presence of a warm absorber in PG 1211+143.

3.4. Emission Components

In addition to the absorption zones, two zones of emission are required to fit the soft X-ray emission lines present in PG 1211+143, where the strongest emission features are marked by red labels in Figure 5. Note that higher-turbulence ($b = 3000 \text{ km s}^{-1}$) grids were used to match the higher-velocity broadening of the emission features. The exception to this is the narrow O VII forbidden line at 22.1 Å, which has instead been modeled with a separate narrow Gaussian profile. Given the lower-velocity width of this line (Table 3), it may be associated with more distant gas at pc scales or greater. A similar (but weak) narrow component of emission may also be associated with N VII Ly α at 24.8 Å.

The two zones correspond to low- and high-ionization gas with ionization parameters of $\log \xi = 2.0$ and $\log \xi = 3.4$, respectively (see Table 4 for details of the emission zones). These zones may be ascribed to the reemission from the corresponding absorption zones 1a and 1b with similar ionization parameters, while the column density of the

emission zones has been tied to the corresponding absorption zone for simplicity. The two emission zones are both significant ($\Delta\chi^2 = 52.4$ and 21.7 for the low- and high-ionization zones, respectively) and are able to reproduce the soft X-ray emission features, such as the broad O VIII Ly α line (see Figure 5). The net velocity of the lower-ionization emission zone is consistent with zero (within $v/c < 0.002c$), while the high-ionization zone prefers a slight blueshift, with $v/c = -0.017 \pm 0.006$. Note that the high-ionization zone predominately contributes toward a “blue wing” of the broad O VIII Ly α emission line, as well some broad Ne IX emission. One possibility is that the soft X-ray lines originate from the reemission from a wide-angle outflow (Pounds & Reeves 2009; Nardini et al. 2015). In this case, the breadth of the emission lines arises from the integration over a range of angles from both the blue and redshifted sides of the wind, with typical velocity widths observed here up to $10,000 \text{ km s}^{-1}$ in the case of the O VIII Ly α line.

3.4.1. The Emitter Covering Fraction

In this framework, the luminosity of the soft X-ray line emission can also be used to calculate the global covering factor of the outflowing gas (see Reeves et al. 2016 for a similar calculation). From the photoionization modeling, the normalization (or flux), κ , of each of the emission components is defined by XSTAR in terms of

$$\kappa = f_{\text{cov}} \frac{L_{38}}{D_{\text{kpc}}^2}, \quad (2)$$

where L_{38} is the 1–1000 Ryd ionizing luminosity in units of $10^{38} \text{ erg s}^{-1}$ and D_{kpc} is the distance to the quasar in kpc. Here f_{cov} is the covering fraction of the gas with respect to the total solid angle, where $f_{\text{cov}} = \Omega/4\pi$ and thus $f_{\text{cov}} = 1$ for a spherical shell of gas. Thus, by comparing the predicted normalization (κ) for a fully covering shell of gas (of column density N_{H}) illuminated by a luminosity, L , versus the observed normalization (κ_{xstar}) determined from the photoionization modeling, the covering fraction of the gas can be estimated.

For PG 1211+143, with $L = 4 \times 10^{45} \text{ erg s}^{-1}$ at a distance of $D = 331 \text{ Mpc}$, and for a spherical shell, the expected XSTAR normalization is $\kappa = 3.7 \times 10^{-4}$. Compared to the observed normalization factors reported in Table 6, the covering fraction of the lower-ionization zone of emitting gas is $f_{\text{cov}} = 0.20 \pm 0.06$ (for a column density of $N_{\text{H}} = 10^{21} \text{ cm}^{-2}$), while the high-ionization zone has a covering fraction of $f_{\text{cov}} = 0.46 \pm 0.20$ (for $N_{\text{H}} = 10^{22} \text{ cm}^{-2}$). This is consistent with the soft X-ray emitting gas covering a substantial fraction of $4\pi \text{ sr}$. This also supports the earlier interpretation of Pounds & Reeves (2009), based on geometrical constraints from the broad emission-line profiles, of a wide-angle outflow in PG 1211+143.

3.5. The Continuum Parameters

With all the absorption and emission components included in the model, the continuum is well described by a soft power-law component with a photon index of $\Gamma = 3.44^{+0.14}_{-0.17}$ and a hard power law of $\Gamma = 1.60 \pm 0.15$. The continuum parameters are summarized in Table 5. Note these continuum parameters are broadly consistent with those obtained from a broadband XMM-Newton and NuSTAR analysis of PG 1211+143 (Lobban

Table 5
Best-fit Continuum Parameters for the Mean PG 1211+143 Spectrum

| Component | Parameter | Value |
|-----------------|------------|------------------------|
| Soft power law | Γ | $3.44^{+0.14}_{-0.17}$ |
| | N_{PL}^a | $1.36^{+0.12}_{-0.09}$ |
| Hard power law | Γ | 1.60 ± 0.15 |
| | N_{PL}^a | $0.74^{+0.06}_{-0.07}$ |
| Galactic column | N_H^b | $6.5^{+1.0}_{-1.2}$ |

Notes.

^a Normalization of the power-law component in units of flux at 1 keV ($\times 10^{-3}$ photons $\text{cm}^{-2} \text{s}^{-1} \text{keV}^{-1}$).

^b Galactic column density in units of $\times 10^{20} \text{cm}^{-2}$.

et al. 2016b). In the final fit, the blackbody component is not required, as noted earlier, and the continuum curvature is well described by the combination of the two power laws. For the above model construction, the absorption zones are applied against the hard power law, whereas the soft power law is unattenuated. If the opposite is assumed to be the case (where the soft power law is absorbed), then the fit statistic obtained is considerably worse ($\Delta\chi^2_\nu = 57.7$), where in this case the shorter-wavelength features such as the Fe M-shell UTA and the 1 keV absorption due to Fe L are underpredicted compared to the longer-wavelength features such as the O-band absorption, which are then overpredicted.

While the model construction is purely phenomenological, the steep power law seems likely to have a physical basis. In an analysis of the spectral variability between earlier (2001, 2004, 2007) *XMM-Newton* spectra, Pounds & Reeves (2009) noted that most of the spectral variability can be accounted for by the steep $\Gamma \sim 3$ power law and that this component, as seen from the difference spectra between observations, appeared to carry little imprint of the ionized absorber in the soft band. Thus, when the spectrum brightened and the soft excess became stronger, the imprint of the absorber became weaker in these archival data. In a variability analysis of the current 2014 *XMM-Newton* data sets, Lobban et al. (2016a) also showed that the long-term (interorbit) variability was also dominated by the steep power-law component, and, when this component is low, the spectrum appears more absorbed. Furthermore, Lobban et al. (2016a) also noted interorbit changes in the strength of the UTA absorption. The interorbit changes of the soft absorber in the RGS spectra are analyzed in Section 4, while some possible physical interpretations of the absorber variability are discussed in Section 5.

4. Outflow Variability

The spectral model from the mean RGS spectrum was used as a template to study the interorbit variability of the soft X-ray spectrum from REV 2652 to REV 2670. Indeed, as shown by Lobban et al. (2016a), the spectral variability of PG 1211+143 is dominated by changes in the soft X-ray band.

Only two of the absorption zones are required in order to fit the sequences from the individual RGS sequences, namely, the low-ionization zone 1a and the high-ionization zone 1b, both of which are outflowing at $-0.06c$ and carry most of the opacity of the absorber. Note that the more tentative

higher-velocity components (zones 2 and 3) are not required to fit the individual sequences given their lower signal-to-noise ratio and so are not included in the template model. Likewise, the emission is also simplified, so that the O VII (forbidden and resonance) and O VIII Ly α lines are fitted with simple Gaussian profiles, as these are the strongest lines that are detected in the individual orbit sequences.

The continuum is modeled in the same way as per the mean spectral analysis, with the combination of the soft and hard power-law components (both of variable normalization). As before, the absorption zones are applied against the hard power law, while the soft power law is assumed to be unattenuated. While a blackbody component was also initially included, its normalization dropped to zero, and thus the continuum can simply be modeled by the combination of the two power laws. The overall form of this simple model is

$$\text{TBABS} \times [\text{XSTAR}_{1a} \times \text{XSTAR}_{1b} \times (\text{POW}_{\text{HARD}}) + \text{POW}_{\text{SOFT}} + \text{GAUSS}],$$

where XSTAR_{1a} and XSTAR_{1b} represent the absorption from zones 1a and 1b, respectively, and GAUSS represents the Gaussian components of the O K-shell emission lines.

The spectral residuals to each sequence against this baseline continuum, prior to including the absorption zones or emission lines, are shown in Figure 7. The second observation (REV 2659) is clearly the most absorbed of the seven spectra, which also coincides with the minimum in soft X-ray flux (e.g., see Figure 2). Conversely, the brightest observation (REV 2664) also appears to be the most featureless in terms of absorption. The most obvious spectral change among the seven spectra corresponds to the UTA, centered around $\sim 15.5 \text{ \AA}$, which shows significant evolution over the course of the campaign. In particular, it increases in strength after the first sequence, reaching maximum opacity during REV 2659 before decreasing again during the subsequent observations (timescale of \sim days) and then becoming largely featureless when the source brightens toward a maximum flux (i.e., REV 2664–2666). To help visualize the spectral variations, we show the count-rate spectra for three of the sequences (REV 2659, 2661, 2664) in Figure 8, coinciding with the increase in continuum flux and having been fitted with the best-fitting variable column density XSTAR model described below. This shows the spectral evolution from lowest to highest soft X-ray flux as the source changes from being absorption-dominated to continuum-dominated and largely featureless. The clearest visualization of this is again in the UTA, whose strength diminishes as the source brightens. With the principal soft-band spectral changes established, we now proceed to fit the seven RGS sequences.

4.1. Column Variability

We first investigated whether the interorbit variability could arise from changes in the column density of the absorber over the course of the seven observations. To test this, we allowed the column density to vary between the seven sequences while tying the ionization parameter, ξ , and redshift (and therefore outflow velocity) of each absorber together across all seven orbits. We also tied the photon indices of the power laws together across observations, along with the centroid energies and widths of the Gaussian emission lines. Thus, the only parameters allowed to vary across the seven sequences are the

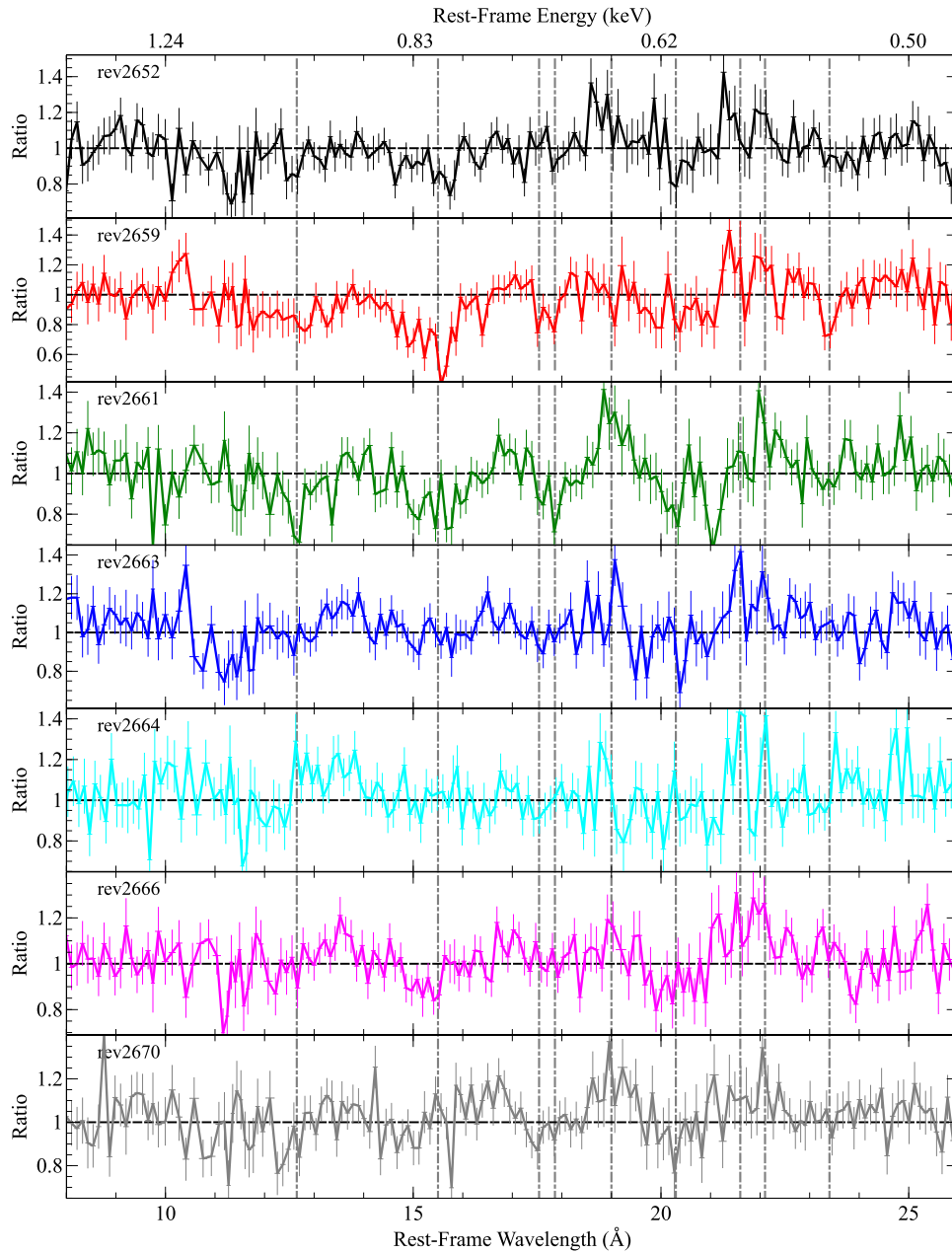


Figure 7. Ratio of the residuals of the seven RGS spectra to the baseline continuum model. The vertical dot-dashed lines correspond to the centroids of Ne IX $1s \rightarrow 2p$ (~ 12.6 Å), Fe M UTA (~ 15.5 Å), O VII $1s \rightarrow 3p$ (~ 17.6 Å), O VIII $1s \rightarrow 2p$ (~ 17.9 Å), O VIII Ly α emission (~ 19 Å), O VII $1s \rightarrow 2p$ (~ 19.2 Å), O VII He α emission (~ 21.6 and ~ 22.1 Å), and N VII $1s \rightarrow 2p$ (~ 23.3 Å). Of the seven spectra, REV 2659 shows the strongest absorption coinciding with the minimum in soft X-ray flux. Notice, in particular, the evolution of the UTA, which is at its maximum depth during REV 2659 but then is not present during REV 2664–2666, when the continuum flux reaches a maximum. Note also the strong variability of the O VIII Ly α emission line, which is strongest in REV 2661, two orbits after the decline in flux.

column densities of the two absorbers, the normalizations of the two power laws, and the flux of the strong O VIII Ly α emission line (as described later).

The joint multi-orbit fit is good ($\chi^2_\nu = 4\,592/4\,262$), with the bulk of the interorbit variability well accounted for by the variations in the column density. In addition, the intrinsic continuum flux increases from REV 2659 (minimum) to REV 2664 (maximum), which is reflected by the increase in the normalization of the soft power-law component, while the column density simultaneously decreases (see Table 6 for parameters). Note that there is no statistical requirement to vary

the outflow velocity across the sequences, and this was subsequently tied for all the spectra.

Note that the improvement in the fit statistic for adding both absorption zones is considerable; measured across the seven sequences then $\Delta\chi^2 = -340$ for zone 1a and $\Delta\chi^2 = -111$ for zone 1b. In Figure 9, we show the model fitted to the two most absorbed spectra, REV 2659 and REV 2661, and, by contrast, the least-absorbed spectrum, REV 2664. It can be seen that the model accounts for the Fe M-shell UTA (~ 15.5 Å) along with the strongest discrete absorption lines—e.g., from O VII and O VIII Ly α . The variable strength of the UTA can be seen

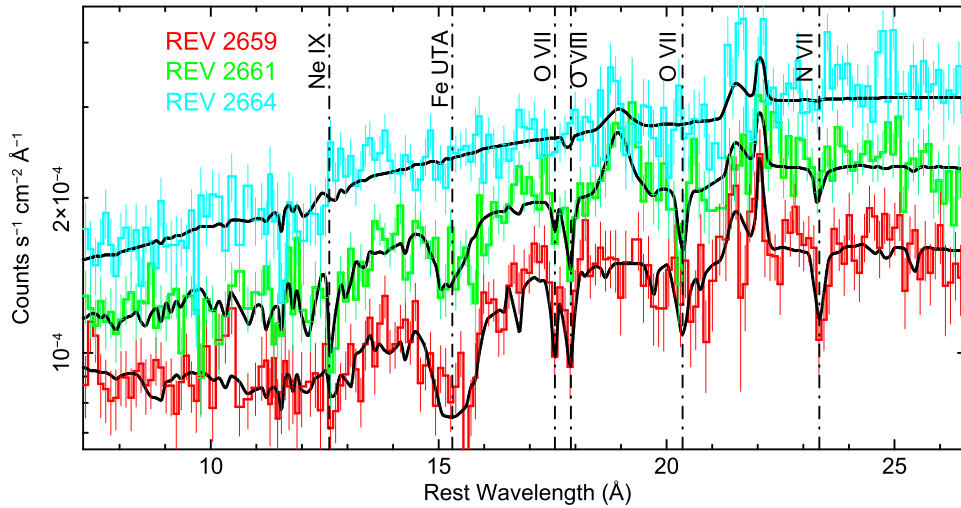


Figure 8. Count-rate RGS spectra, showing REV 2659 (red), REV 2661 (green), and REV 2664 (cyan), where the spectral changes are most apparent. Data are shown as histograms with 1σ errors, and the best-fitting XSTAR model to each sequence is shown as a solid line. The spectra are plotted following the increase in flux from REV 2659 (minimum) to REV 2664 (maximum), where the soft X-ray spectrum evolves from strongly absorbed to continuum-dominated. In particular, the decrease in opacity of the UTA (~ 15.5 Å), O VIII Ly α (17.9 Å), O VII He α (20.3 Å), and N VIII Ly α (23.4 Å) absorption features (dot-dashed lines) over time is clearly apparent.

between the three orbits and is accounted for by variations in the column density of the absorber.

The column density variations across the seven observations are listed in Table 6 and plotted in Figure 10 (panels (a) and (b)). The column densities of both zones appear to vary by up to an order of magnitude across all seven observations, in addition to the changes in the normalizations of the power-law continuum components. The variations in the column density of the lower-ionization zone 1a appear to inversely track the flux behavior of the source, with the column reaching a maximum value of $N_{\text{H}} = 5.7^{+2.0}_{-1.6} \times 10^{21} \text{ cm}^{-2}$ when the observed flux is weakest in REV 2659. Conversely, the minimum column density occurs during the brighter sequences—e.g., REV 2664, with only an upper limit of $N_{\text{H}} < 1.1 \times 10^{20} \text{ cm}^{-2}$. The high column of REV 2659 corresponds to an increase in the strength of the UTA at around $\sim 15\text{--}16$ Å, whereafter the column density decreases over the subsequent observations as the source flux increases. The variability of the absorber is observed to be rapid, with the column density of zone 1a decreasing by a factor of ~ 5 from REV 2659 to REV 2661—a period of just ~ 4 days. The changes in absorber opacity versus flux can clearly be seen by comparing the respective panels of Figure 10 (panels (a) and (b) versus (e)).

Similar behavior is observed in the higher-ionization zone 1b, with an increase in the column density required to match an increased strength in high-ionization absorption lines when the source flux is lower. However, in the case of zone 1b, the column density actually peaks during REV 2661 ($N_{\text{H}} = 2.6^{+1.6}_{-1.0} \times 10^{22} \text{ cm}^{-2}$) and thus is delayed in its response to the variable source continuum with respect to the lower-ionization zone 1a, where the column density peaks a couple of orbits earlier. This behavior is also apparent in Figure 9, where the REV 2661 spectrum shows strong highly ionized absorption lines due to O VII, O VIII, and Ne IX, whereas in REV 2659, the low-ionization Fe UTA is at its strongest. This might imply two separate obscuration events occurring along the line of sight that are spatially independent or a cospatial two-phase medium whereby the high-ionization absorber reacts differently to the lower-ionization gas. Nevertheless, in both cases, the column

densities further decrease when the observed source continuum flux reaches its maximum value around REV 2664–2666—i.e., imprinting minimal features onto what becomes a largely featureless soft X-ray spectrum.

4.2. Covering Fraction Variations

Given the rapid variability of the column density of the absorbing gas in PG 1211+143, it seems plausible that the increase in opacity around REV 2659 could arise from the passage of patchy absorbing clouds or clumps of gas into our line of sight as part of an inhomogeneous wind. This can be tested by modeling the opacity changes by a variable partially covering absorber, such that part of the continuum leaks through a patchy medium and only part is attenuated. For this purpose, the model construction is altered such that

$$\text{TBABS} \times [c_1 \times \text{XSTAR}_{1a} \times \text{XSTAR}_{1b} \times (\text{POW}_{\text{HARD}} + \text{POW}_{\text{SOFT}}) + c_2 \times (\text{POW}_{\text{HARD}} + \text{POW}_{\text{SOFT}}) + \text{GAUSS}],$$

where the covering fraction is then $f_{\text{cov}} = c_1/(c_1 + c_2)$ and the other components are as before. The column densities are tied across the seven sequences (zone 1a, $N_{\text{H}} = 5.4^{+1.9}_{-1.2} \times 10^{21} \text{ cm}^{-2}$; zone 1b, $N_{\text{H}} = 3.7^{+3.1}_{-1.2} \times 10^{22} \text{ cm}^{-2}$), while the ionizations and velocities of the two zones are also tied with values found to be consistent from before. Note that the relative power-law normalizations vary between sequences, and thus the flux is allowed to be intrinsically variable. The resulting covering fraction variations are plotted in panel (c) of Figure 10 and listed in Table 6; these vary from the highest covering during REV 2659 ($f_{\text{cov}} = 0.47^{+0.05}_{-0.04}$) to lowest during the featureless REV 2664 ($f_{\text{cov}} < 0.08$) spectrum.

The covering fraction is found to be inversely proportional to the quasar flux (panel (c) versus panel (e)), and thus the quasar is most absorbed when it is faintest. Note that the absorber variations are similar to those found for the variable column density case, while the fit statistic is virtually identical with $\chi^2_{\nu} = 4589/4259$. This is not surprising, as, in practice, variations in the covering factor (for a given cloud column

Table 6
Best-fitting Model Parameters from the Multi-orbit RGS Fit, Fitted with Either Variable Column Density or Variable Covering Fraction

| Obs. | N_{H}^{a} (Zone 1a) | N_{H}^{b} (Zone 1b) | $F_{\text{cov}}^{\text{c}}$ | N^{d} (POW _{HARD}) | N^{d} (POW _{SOFT}) | $F_{0.4-2 \text{ keV}}^{\text{e}}$ |
|----------|-------------------------------------|-------------------------------------|-----------------------------|---------------------------------------|---------------------------------------|------------------------------------|
| REV 2652 | $4.21_{-2.23}^{+3.04}$ | $2.22_{-2.22}^{+3.80}$ | $0.17_{-0.05}^{+0.05}$ | $7.31_{-0.65}^{+0.66}$ | $10.07_{-0.69}^{+0.69}$ | $5.39_{-0.09}^{+0.10}$ |
| REV 2659 | $56.8_{-16.1}^{+19.8}$ | $6.71_{-5.63}^{+1.05}$ | $0.47_{-0.04}^{+0.05}$ | $7.40_{-0.78}^{+0.87}$ | $6.61_{-0.51}^{+0.49}$ | $3.43_{-0.07}^{+0.06}$ |
| REV 2661 | $11.1_{-3.52}^{+6.14}$ | $25.8_{-9.79}^{+16.0}$ | $0.30_{-0.05}^{+0.04}$ | $7.59_{-0.78}^{+0.86}$ | $9.89_{-0.62}^{+0.67}$ | $4.84_{-0.09}^{+0.09}$ |
| REV 2663 | $<3.33^{\text{p}}$ | $13.1_{-7.08}^{+13.3}$ | $0.14_{-0.06}^{+0.05}$ | $6.39_{-0.72}^{+0.76}$ | $10.62_{-0.64}^{+0.66}$ | $5.50_{-0.08}^{+0.07}$ |
| REV 2664 | $<1.14^{\text{p}}$ | $3.34_{-2.25}^{+4.87}$ | <0.08 | $7.53_{-0.79}^{+0.86}$ | $14.72_{-0.76}^{+0.78}$ | $6.75_{-0.11}^{+0.11}$ |
| REV 2666 | $5.67_{-4.00}^{+2.94}$ | $3.03_{-3.02}^{+3.20}$ | $0.11_{-0.05}^{+0.05}$ | $6.15_{-0.67}^{+0.68}$ | $15.21_{-0.70}^{+0.71}$ | $6.37_{-0.08}^{+0.08}$ |
| REV 2670 | $4.31_{-3.24}^{+2.26}$ | $15.2_{-7.0}^{+11.9}$ | $0.20_{-0.05}^{+0.05}$ | $6.45_{-0.71}^{+0.75}$ | $10.64_{-0.65}^{+0.66}$ | $5.05_{-0.07}^{+0.08}$ |

Notes.

^a The column density of zone 1a (with constant $\log \xi = 1.8 \pm 0.1$; $v/c = -0.060 \pm 0.001$) in units of $\times 10^{20} \text{ cm}^{-2}$. ^p denotes that the column density is at the lowest value allowed by the model (i.e., 10^{19} cm^{-2}).

^b The column density of zone 1b (with constant $\log \xi = 3.3 \pm 0.1$; $v/c = -0.062 \pm 0.001$) in units of $\times 10^{21} \text{ cm}^{-2}$.

^c Variable covering fraction of gas, with constant column density and ionization.

^d The observed flux from 0.4–2 keV in units of $\times 10^{-12} \text{ erg cm}^{-2} \text{ s}^{-1}$.

^e The normalization of the specified power-law component in units of $\times 10^{-4} \text{ photons cm}^{-2} \text{ s}^{-1}$.

density) will be indistinguishable from the equivalent variations in column density (for a given covering) of the absorber. The line-of-sight column/covering variations are discussed further in Section 5.2.

4.3. Continuum Variations Only

As a further consistency check, we also attempt to see whether the spectral changes between the sequences can be accounted for purely by continuum variability of the soft versus hard power-law components. In the original model construction, only the direct hard power law is absorbed, while the soft power law is unattenuated; thus, it may be possible to mimic the opacity changes by an increase in the soft component relative to a less variable hard power-law component. For instance, in the lowest-flux spectrum (REV 2659), the soft flux is low and the spectrum appears more absorbed, while in the brightest sequences (e.g., REV 2664), the flux of the soft component strongly increases with respect to the hard power law. Indeed, such a behavior was noted in the *Chandra* observations of the Seyfert 1 galaxy NGC 3783 (Netzer et al. 2003), where, although no changes in the warm absorber were observed, a featureless soft component was found to vary between the observations.

To test this, we tied the column densities of the two absorbers across all seven sequences, allowing only the normalizations of the respective soft versus hard power-law components to vary between the seven orbits. However, the result was a substantially worse fit compared to the variable column density case (where both the continuum normalizations and the column densities were allowed to vary across all the data sets). Indeed, the fit statistic worsens to $\chi^2_{\nu} = 4\,742.9/4\,274$, resulting in a $\Delta\chi^2 = +151.5$ for 12 extra degrees of freedom. Such an increase in the fit statistic is strongly ruled out with a null hypothesis probability of 1.5×10^{-23} , and thus continuum variations alone cannot explain the spectral variability across the seven observations of PG 1211+143. In particular, this scenario fails to reproduce the strong changes around the Fe M-shell UTA, which is observed from REV 2659 to REV 2664.

4.4. Ionization Variability

While pure continuum variability is ruled out, we tested whether the interorbit variability could be due to the variability of the absorber ionization in response to the variable continuum, instead of being driven by large column changes. Thus, the column density of each absorber was tied to the same value across all seven orbits for both zones 1a and 1b, while the ionization was allowed to vary instead. However, the resulting fit statistic was found to be worse by $\Delta\chi^2 = 40$ compared to the above variable column density scenario. In particular, variations in ionization alone cannot reproduce the increase in strength of the UTA arising from the low-ionization (zone 1a) absorber, which instead requires a significant increase in column, especially during the low-flux REV 2659 sequence.

Thus, the variability of the low-ionization absorber appears primarily driven by column density changes, although the variability of the high-ionization absorber may still be accounted for by variable ionization. To test this hybrid scenario, we allowed the ionization parameter to vary for the high-ionization (zone 1b) absorber (with a constant column density), while, conversely, the column density of the low-ionization (zone 1a) absorber was allowed to vary as before (and assuming a constant ionization parameter). This gave a better fit, with $\chi^2_{\nu} = 4\,590/4\,262$, statistically equivalent to the purely variable column density case from Section 4.1. Here the column density of the low-ionization absorber varies as above, but the ionization parameter of the highly ionized absorber appears to track the soft X-ray continuum variability, which can be seen from comparing panels (d) and (e) in Figure 10.

The resulting ionization changes for zone 1b are shown in Figure 10 (panel (d)) and listed in Table 7, with the ionization parameter at its lowest value of $\log \xi = 3.02 \pm 0.10$ during REV 2661, when the high-ionization absorption lines appear strongest in the RGS spectrum, as is apparent in Figure 9. Subsequently, the absorber ionization increases when the continuum flux reaches its maximum value during REV 2664 and REV 2666, with $\log \xi = 3.40_{-0.07}^{+0.16}$ in the former sequence. The increase in ionization parameter leads to the high-ionization absorber becoming more transparent, and, hence, the higher-flux sequences are relatively featureless. Note that the magnitude of the changes in ionization for zone 1b are

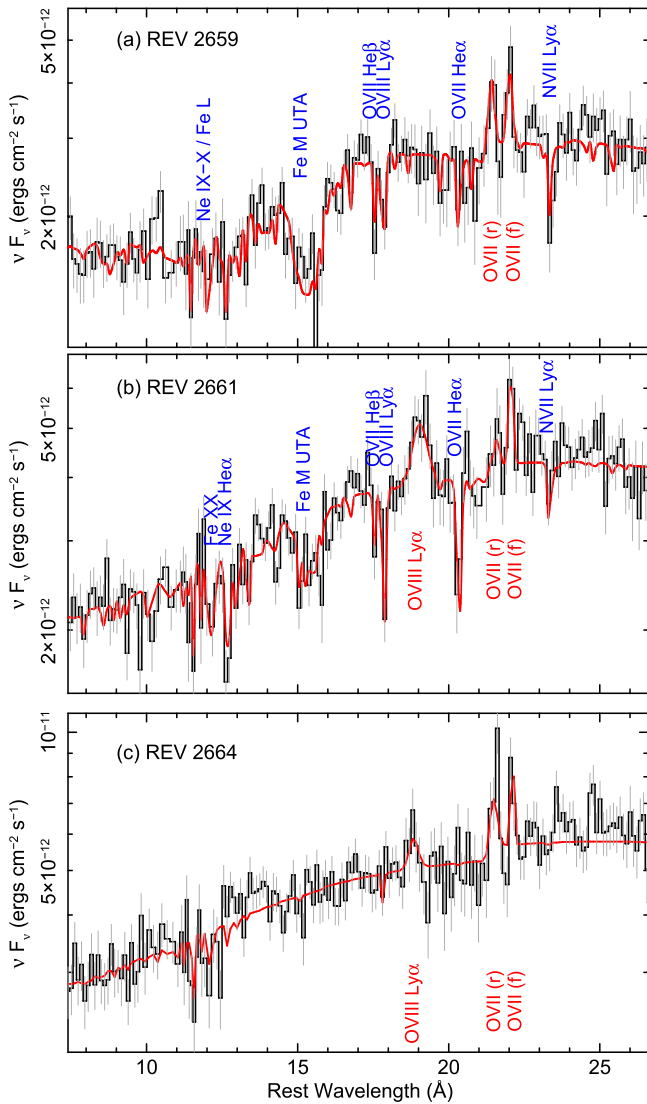


Figure 9. Best-fitting two-zone XSTAR model (red line) fitted to the RGS spectra of PG 1211+143 during the rise in quasar flux from (a) REV 2659, to (b) REV 2661, to (c) REV 2664. The spectra are fitted allowing the column densities and continuum normalizations to vary between orbits. During REV 2659, the low-ionization absorber (zone 1a) is at its deepest, which can be seen in the form of the deep Fe M-shell UTA at ~ 15 Å. In REV 2661, the depth of the low-ionization UTA decreases, although strong, high-ionization absorption lines from O VII, O VIII, and Ne IX are still apparent from the higher-ionization zone 1b. Then, in REV 2664, when the quasar flux is at its maximum, the column density has decreased, with only a trace amount of high-ionization iron L-shell absorption present. Note the increase in flux of the broad O VIII Ly α emission line at 19 Å as the quasar flux increases from REV 2659 to REV 2661 and then the subsequent decline in REV 2664 at the maximum continuum flux.

roughly in proportion to the changes in continuum flux, with the latter increasing by a factor of 2 from REV 2659 to REV 2664. There may also be some indication of a delay in the ionization in response to the continuum variability, with the minimum in ionization occurring during REV 2661 when the continuum flux has already started to increase, while the minimum in flux occurs ~ 2 *XMM-Newton* orbits earlier during REV 2659. This can be seen from comparing panels (d) and (e) in Figure 10.

In summary, the variability of the low-ionization absorber is most likely to be accounted for by changes in column density

(or, equivalently, covering fraction), with the quasar most absorbed during the low-flux REV 2659 observation. On the other hand, the variability of the high-ionization absorber can be equally well explained by either an increase in column density centered on REV 2661 or changes in the absorber ionization in response to the variable soft X-ray continuum.

Finally, we note that, in emission, the broad O VIII Ly α line appears highly variable, with the line fluxes and equivalent widths (EWs) listed for each sequence in Table 7. Note that no significant variability is observed in the O VII emission by comparison, although the larger errors preclude a direct comparison. In particular, the O VIII emission-line flux drops in the low-flux REV 2659 spectrum and then increases two orbits later (in REV 2661) as the continuum flux rises, which is visible in Figure 9. Quantitatively, the line flux (and EW) varies from $< 1.2 \times 10^{-5}$ photons $\text{cm}^{-2} \text{s}^{-1}$ (EW < 2.0 eV) to $4.8 \pm 1.1 \times 10^{-5}$ photons $\text{cm}^{-2} \text{s}^{-1}$ (EW = 6.0 ± 1.4 eV) between these two orbits. However, in the subsequent orbits (e.g., REV 2664), as the continuum continues to rise, the line flux (and EW) appear to decrease. Thus, the emission line does not directly respond in proportion to the continuum, as might be expected in a simple reverberation scenario, which would lead to a constant EW of the emission line. Alternatively, as is discussed in Section 5.2, the increase in line flux in REV 2661 may be explained in terms of a delay due to recombination following the earlier drop in continuum flux centered on REV 2659. In the subsequent orbits, the decline in the emission-line strength may then be due to an increase in the ionization in response to the rise in the continuum flux.

5. Discussion

5.1. Comparison to Other Fast Soft X-Ray Outflows

We have carried out a detailed analysis of the deep 2014 *XMM-Newton* RGS observations of the ultrafast outflow in PG 1211+143, finding a number of blueshifted absorption lines with a common outflow velocity of $\sim -0.06c$. We note that recently, Kriss et al. (2018) discovered a UV component of the fast outflow of PG 1211+143 from the detection of a Ly α trough, where the strongest component has an outflow velocity of -17420 ± 15 km s^{-1} . This compares to the main zone 1a and 1b components of the wind found in this RGS analysis (Section 3.2), which have respective outflow velocities of $-0.062 \pm 0.001c$ (or -18600 ± 300 km s^{-1}) and $-0.059 \pm 0.002c$ (or -17700 ± 600 km s^{-1}). In particular, the UV absorption-line system measured by Kriss et al. (2018) is consistent within the errors with the velocity of the zone 1b absorber measured here. Furthermore, an analysis of the simultaneous *Chandra* HETG observations of PG 1211+143 by Danehkar et al. (2018), taken 1 yr later compared to the 2014 *XMM-Newton* observations, also confirms the detection of the $-0.06c$ component of the fast soft X-ray outflow through the presence of absorption lines detected in the Ne, Mg, and Si bands.

While the most ultrafast outflows have been detected in the iron K band through high-ionization lines of Fe XXV or Fe XXVI (Tombesi et al. 2010; Gofford et al. 2013), PG 1211+143 is one among a small number of AGNs with sufficient exposure with X-ray gratings, where components of an ultrafast outflow have also been detected in the soft X-ray band (Pounds 2014a; Pounds et al. 2016b). Now, both the current *XMM-Newton* analysis and the *Chandra* analysis of Danehkar et al. (2018) confirm the

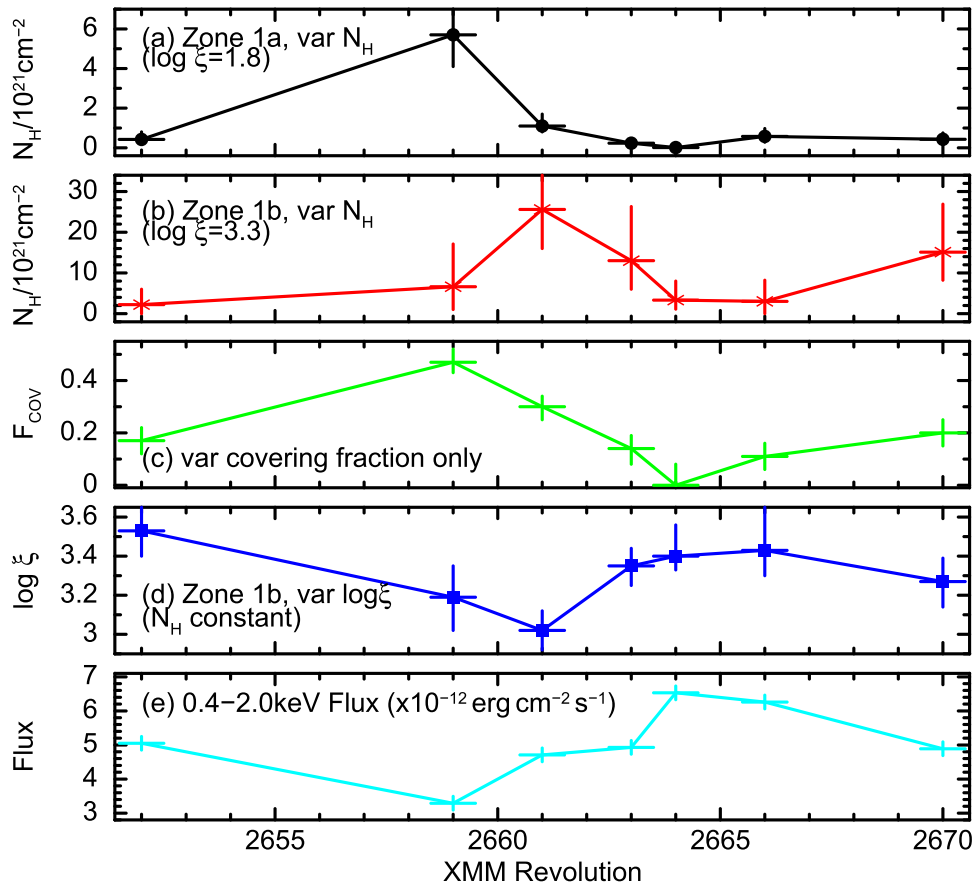


Figure 10. Variability of the two high-opacity absorbers (zones 1a and 1b) across the seven *XMM-Newton* RGS observations (see Tables 6 and 7 for details of the absorber variability). Panel (a) shows the variations in column density for the low-ionization zone 1a, which reaches its peak in REV 2659 during the low-flux episode, ~ 15 days into the campaign. The column then rapidly declines in subsequent orbits as the quasar flux increases. Panel (b) shows a similar behavior for the high-ionization zone 1b, except here, the column density reaches a maximum two orbits later during REV 2661. Panel (c) shows the absorber variations instead expressed in terms of a variable covering fraction but assuming a constant column and ionization across the seven sequences. Note that the covering fraction anticorrelates with the flux in panel (e). Panel (d) shows the zone 1b variations, where the absorber variations have been fitted with a variable ionization parameter but a constant column density. This may indicate that the high-ionization absorber reacts to changes in the soft X-ray continuum, reaching a minimum ionization shortly after the decline in continuum quasar flux shown in panel (e).

Table 7
Best-fitting Model Parameters for the High-ionization Zone 1b Absorber, When the Ionization Parameter Is Allowed to Vary between the Seven Observations

| Obs. | $\log \xi$ | O VIII Flux ^a | O VIII EW ^b | $F_{0.4-2 \text{ keV}}$ ^c |
|----------|------------------------|--------------------------|------------------------|--------------------------------------|
| REV 2652 | $3.53^{+0.17}_{-0.13}$ | $3.3^{+1.2}_{-1.2}$ | $4.0^{+1.5}_{-1.5}$ | $5.39^{+0.10}_{-0.09}$ |
| REV 2659 | $3.19^{+0.16}_{-0.17}$ | <1.2 | <2.0 | $3.43^{+0.06}_{-0.07}$ |
| REV 2661 | $3.02^{+0.10}_{-0.10}$ | $4.8^{+1.1}_{-1.1}$ | $6.0^{+1.4}_{-1.4}$ | $4.84^{+0.09}_{-0.09}$ |
| REV 2663 | $3.35^{+0.09}_{-0.10}$ | $1.8^{+1.1}_{-1.1}$ | $2.2^{+1.3}_{-1.3}$ | $5.50^{+0.07}_{-0.08}$ |
| REV 2664 | $3.40^{+0.16}_{-0.07}$ | $1.4^{+1.5}_{-1.4}$ | $1.3^{+1.4}_{-1.3}$ | $6.75^{+0.11}_{-0.11}$ |
| REV 2666 | $3.43^{+0.22}_{-0.13}$ | $1.7^{+1.2}_{-1.2}$ | $1.6^{+1.1}_{-1.1}$ | $6.37^{+0.08}_{-0.08}$ |
| REV 2670 | $3.27^{+0.12}_{-0.13}$ | $2.8^{+1.1}_{-1.1}$ | $3.3^{+1.3}_{-1.3}$ | $5.05^{+0.08}_{-0.07}$ |

Notes. Note here that the column density has been tied across seven observations, with a best-fitting value of $N_{\text{H}} = 7.0^{+3.0}_{-2.0} \times 10^{21} \text{ cm}^{-2}$.

^a The flux of the high-ionization O VIII Ly α emission line, which appears to vary between orbits, in units of $\times 10^{-5} \text{ photons cm}^{-2} \text{ s}^{-1}$. Note that the highest O VIII flux coincides when the ionization of the absorber is lowest, during REV 2661.

^b The EW of the O VIII Ly α emission line in units of eV.

^c The observed 0.4–2 keV flux in units of $\times 10^{-12} \text{ erg cm}^{-2} \text{ s}^{-1}$.

presence of a fast soft X-ray wind in PG 1211+143 with consistent velocities. Examples of fast soft X-ray outflows in

other AGNs include the luminous nearby quasar PDS 456 (Reeves et al. 2003, 2016); the NLS1s IRAS 17020+4544 (Longinotti et al. 2015), IRAS 13224+3809 (Parker et al. 2017; Pinto et al. 2017b), and Ark 564 (Gupta et al. 2013); and the Seyfert 1 galaxy Mrk 590 (Gupta et al. 2015).

Of these AGNs, the NLS1 IRAS 17020+4544 (Longinotti et al. 2015) may bear the closest resemblance to PG 1211+143, in terms of the complexity of the soft X-ray outflow. PG 1211+143 shows clear contributions from both low- and high-ionization zones of the fast soft X-ray absorber, covering two orders of magnitude in ionization, where the imprint of the outflow ranges from the low-ionization Fe M-shell UTA to H-like absorption from N, O, and Ne. Likewise, the outflow in IRAS 17020+4544 also exhibits a wide range in ionization, especially in the O K-shell band, with significant low-ionization absorption occurring from the inner shell lines of O III–VI, with higher-ionization absorption from O VII–VIII also being present. Longinotti et al. (2015) discussed the fast but low-ionization absorption as arising from either a clumpy wind or the immediate postshock gas following interaction of a faster (more ionized) wind component with circumnuclear gas (see King 2010). The observed outflow velocity is also similar to PG 1211+143, with possible multiple velocity components

ranging from $-23,600$ to $-27,200 \text{ km s}^{-1}$ for the three most significant zones.

In contrast to IRAS 17020+4544, where a spread of velocities may be observed, in PG 1211+143, most of the absorption from both the low- and high-ionization gas originates from lines found with a common mean velocity of $-0.062 \pm 0.001c$ (or $-18600 \pm 300 \text{ km s}^{-1}$) and subsequently confirmed from the XSTAR analysis in Section 3.2 (see Table 4, absorber zones 1a and 1b). There is some indication in the 2014 data of a slightly higher-velocity component, with $v = -0.077 \pm 0.001c$ (or $-23100 \pm 300 \text{ km s}^{-1}$) for the zone 2 absorber. In the spectrum, this is seen in the form of a second absorption-line component observed blueward of the O VII He α and O VIII Ly α line profiles (Figure 5). Although weak, this latter component is consistent with the main velocity component measured in the 2001 *XMM-Newton* observation of $-23170 \pm 300 \text{ km s}^{-1}$ (Pounds 2014a). This is formally lower than the systemic velocity of PG 1211+143 (of $-24,300 \text{ km s}^{-1}$) and so probably does not originate from Galactic absorption.

As we have seen in Section 4, the seven 2014 *XMM-Newton* sequences do show pronounced variability in the absorber opacity, in addition to an intrinsically variable continuum. This may be interpreted in terms of variations in either column density, covering fraction, or ionization changes, occurring on timescales of days. Indeed, PG 1211+143 appears to follow the same trend as seen toward the soft X-ray outflows in both PDS 456 and IRAS 13224+3809, where the absorber opacity diminishes with increasing luminosity. In IRAS 13224+3809, Pinto et al. (2017b) recently showed that the absorption lines from the fast outflow seen in both the soft X-ray and Fe K bands decreases in strength with increasing continuum flux; this was attributed to the increasing ionization state of the wind, with the absorber essentially becoming transparent at high fluxes. Likewise, in PG 1211+143, the soft X-ray spectrum becomes featureless in the highest-flux sequences, such as in REV 2664 and REV 2666. In PDS 456, Reeves et al. (2016) also found that the broad absorption profiles seen in the RGS data were generally stronger when the quasar was more absorbed and in a lower flux state, with the soft X-ray absorber changes attributed to a variable column density or covering fraction. The soft X-ray phase of the wind in PDS 456 was interpreted as arising from denser clumps of material located within the fast wind. Furthermore, in the iron K band, the strength of the ultrafast outflow in PDS 456 appears to be anticorrelated with the continuum, as seen from a principal components analysis of the archival *XMM-Newton* observations (Parker et al. 2018). Similar to IRAS 13224+3809, this finding may be interpreted in terms of the wind ionization reacting to the continuum flux.

In PG 1211+143, the new *XMM-Newton* observations appear to have resolved an absorption event centered on REV 2659, the most absorbed sequence of the long-look campaign. Next, we investigate the constraints that the absorber variability and timescales provide on the properties of the soft X-ray absorber in PG 1211+143.

5.2. Location and Properties of the Outflowing Gas

The variability of the soft X-ray absorber can be used to deduce the properties and location of the outflowing gas in PG 1211+143. The rapid variability of the column density (or covering fraction) for the low-ionization (zone 1a) absorber suggests that this phase of the outflow is highly

inhomogeneous. We can attribute the increase in column density around REV 2659 to the passage of an absorbing cloud or filament across our line of sight. In that case, the timescale of the absorption event can give an estimate of the size scale (ΔR) of the absorber as $\Delta R = v_t \Delta t$, where v_t is the transverse velocity of the absorber across our line of sight. While the transverse velocity is not known (but is likely to be smaller than the outflow velocity along the direct line of sight), as a first approximation, this can be set equal to the Keplerian velocity at a radius R , where $v_t = (GM/R)^{1/2}$. Thus,

$$\Delta R = \left(\frac{GM}{R} \right)^{1/2} \Delta t. \quad (3)$$

The radius, R , is related to the ionization parameter and electron density of the absorber as $R^2 = L/n_e \xi$, where L is the 1–1000 Ryd ionizing luminosity. The electron density is also related to the absorber size scale as $n_e = \Delta N_H / \Delta R$, where ΔN_H is the change in column density measured from the observations.

Combining these expressions then gives, for the radial location of the absorber, R ,

$$R^{5/2} = (GM)^{1/2} \frac{L \Delta t}{\Delta N_H \xi}. \quad (4)$$

The change in the column density of the low-ionization absorber is $\Delta N_H = 5 \times 10^{21} \text{ cm}^{-2}$, occurring over a timescale of approximately two *XMM-Newton* orbits or $\Delta t = 300 \text{ ks}$, i.e., as measured from the decline of the column density from REV 2659 to REV 2661 (see Figure 10; panel (a)). The ionizing luminosity of PG 1211+143 from the measured optical to X-ray SED is $L = 4 \times 10^{45} \text{ erg s}^{-1}$ (Lobban et al. 2016a), while the ionization of the gas is $\log \xi = 1.8$ (Table 6). We assume a black hole mass of $M = 10^8 M_\odot$, which is within the range of the reverberation mass estimates for PG 1211+143 of $0.4\text{--}1.5 \times 10^8 M_\odot$ (Kaspi et al. 2000; Peterson et al. 2004). Thus, while there is some uncertainty in the exact black hole mass of PG 1211+143, the above radius is only a weak function of the mass (i.e., $R \propto M^{1/5}$).

For the above values, the estimated radial distance of the low-ionization (zone 1a) absorber is $R = 7 \times 10^{17} \text{ cm}$ or $\sim 10^{18} \text{ cm}$. From this, the corresponding density is $n_e = L/\xi R^2 \sim 10^8 \text{ cm}^{-3}$, and the absorber size scale is $\Delta R = \Delta N_H / n_e \sim 5 \times 10^{13} \text{ cm}$, while the transverse velocity of absorber clouds is then $v_t = 1500 \text{ km s}^{-1}$. Thus, in order to reproduce the rapid increase in the column of the low-ionization absorber centered on REV 2659, the absorbing clouds have to be compact (a few gravitational radii in extent), relatively dense ($n_e \sim 10^8 \text{ cm}^{-3}$), and highly inhomogeneous (with $\Delta R/R \sim 10^{-4}$).

The same argument can also be used to estimate the size scale and location of the high-ionization (zone 1b) absorber from the column density variations presented earlier in Section 4.1. In this case, $\Delta N_H = 2 \times 10^{22} \text{ cm}^{-2}$ and $\Delta t = 500 \text{ ks}$ from the decline of zone 1b of the absorber from REV 2661 to REV 2664 (three *XMM-Newton* orbits), while the ionization is $\log \xi = 3.3$. Hence, from Equation (4), $R = 7 \times 10^{16} \sim 10^{17} \text{ cm}$ and, subsequently, $n_e \sim 3 \times 10^8 \text{ cm}^{-3}$, $\Delta R \sim 10^{14} \text{ cm}$, and the transverse velocity is then $v_t = 4000 \text{ km s}^{-1}$. Thus, the absorber location is an order of magnitude closer to the black hole, which may be expected

given the higher ionization of this zone and similar density to the above. Note that the derived transverse velocity is then $v_t = 4000 \text{ km s}^{-1}$, which is not inconsistent with the measured velocity widths of the soft X-ray emission lines in the PG 1211 +143 spectrum.

5.3. A Two-phase Outflow?

The above argument suggests that the low- and high-ionization absorbers could arise from gas at two different radial locations, with the higher-ionization gas closer in. However, if the two absorber zones were physically unconnected, it might seem coincidental that the increase in absorption is seen from both zones during this campaign unless they both move into the line of sight at around the same time. Furthermore, given the identical outflow velocities (consistent with $-0.06c$ within errors) of these two absorption zones, it may instead be more plausible that the absorbers exist cospatially within a two-phase medium.

To test this, we consider a scenario whereby the ionization of the more highly ionized medium responds directly to the continuum and where any delay in the response of the absorber following a decrease in the continuum level might arise as a result of the recombination timescale of the gas. As per Section 4.4, in this case, we assume any column density variations are negligible, which may be reasonable if the high-ionization gas is less dense and more spatially extended than for the lower-ionization clumps. The density (and thus the gas location) can then be estimated, as it is inversely proportional to the recombination time.

From the analysis in Section 4.4, we found that the change in the ionization parameter of absorption zone 1b may be slightly delayed with respect to the continuum. Here the minimum in the absorber ionization parameter during REV 2661 (Figure 10; panel (d)) occurs when the continuum is already increasing (panel (e)), approximately two *XMM-Newton* orbits after the minimum in the soft X-ray flux during REV 2659. This may be interpreted as a delay due to recombination, with the decrease in ionization following a decrease in ionizing flux. A similar behavior is also seen for the O VIII Ly α emission line, which reaches a maximum intensity in REV 2661 (Table 7), following the earlier minimum in the continuum flux, perhaps arising as a result of a decrease in ionization.

The recombination time can be approximated as $t_{\text{rec}} \sim (\alpha_r n_e)^{-1}$, where α_r is the recombination coefficient for ions recombining into O VIII. We note that the above is only a simplistic approximation for the recombination time, and the resulting densities should only be treated as an order-of-magnitude estimate. From the observations, we estimate $t_{\text{rec}} = 300 \text{ ks}$ (i.e., two *XMM-Newton* orbits) as a realistic recombination time for the highly ionized gas. On the other hand, α_r is dependent on the temperature of the gas. This may be estimated from the observed width of any radiative recombination Continuum (RRC) features in the RGS spectrum, with the best constraints arising from the O VII RRC (see Table 3), with $kT \sim 18 \text{ eV}$. Thus, for $T = 2 \times 10^5 \text{ K}$, $\alpha_r = 7.5 \times 10^{-12} \text{ cm}^3 \text{ s}^{-1}$ (Nahar & Pradhan 2003) and, subsequently, $n_e = 5 \times 10^5 \text{ cm}^{-3}$. Note that the O VIII RRC from the higher-ionization gas (see also Pounds & Reeves 2009) is not so apparent, which may be the case if the temperature of the more highly ionized gas is greater (and thus the RRC is too broad to detect), or it may be blended into the

broad Ne IX emission line. In the former case, for $T = 10^6 \text{ K}$, $\alpha_r = 2.1 \times 10^{-12} \text{ cm}^3 \text{ s}^{-1}$ and $n_e = 1.4 \times 10^6 \text{ cm}^{-3}$.

A plausible estimate for the density of the high-ionization gas is $n_e \sim 10^6 \text{ cm}^{-3}$. Thus, for a mean ionization parameter of $\log \xi = 3.3$, the typical radial distance is $R \sim 10^{18} \text{ cm}$. This is in agreement with the radial estimate derived for the compact low-ionization absorbing clouds. Thus, the data are consistent with a two-phase outflowing medium, whereby the high-density but low-ionization clouds can coexist within a lower-density but higher-ionization medium. In this scenario, both of these absorbers may form part of the same wind streamline outflowing at $-0.06c$.

5.4. Mass Outflow Rate and Energetics

With an estimate of the likely outflow radius and the overall properties of the gas, it is then possible to calculate the possible contribution of the soft X-ray outflow toward the mass outflow rate. This can be expressed in the following form (e.g., see Blustin et al. 2005):

$$\dot{M}_{\text{out}} = 4\pi f_{\text{cov}} \mu m_p v_{\text{out}} f_v n_e R^2. \quad (5)$$

Here f_{cov} corresponds to the global covering factor of the outflow (i.e., as a fraction of $4\pi \text{ sr}$ solid angle), μm_p is the average atomic mass of the gas, and f_v is the volume filling factor along the flow. For a more homogeneous outflow (where $f_v \sim 1$), the above expression can be integrated with respect to radius to instead obtain the mass outflow rate in terms of the column density (e.g., Nardini et al. 2015),

$$\dot{M}_{\text{out}} = 4\pi f_{\text{cov}} \mu m_p v_{\text{out}} N_{\text{H}} R, \quad (6)$$

where R corresponds to the inner radial distance to the wind from the X-ray source.

For the low-ionization (zone 1a) absorber, the material is highly inhomogeneous, as observed from the rapid column changes, and so we estimate the mass outflow rate from Equation (5). From the calculations above, $n_e \sim 10^8 \text{ cm}^{-3}$ and $R \sim 10^{18} \text{ cm}$, while the volume filling factor is $f_v \sim \Delta R/R \sim 10^{-4}$ (i.e., the absorber is in the form of compact clumps). The best estimate of the overall global covering factor comes from the emission associated with this zone, which was calculated from Table 4 to be $f_{\text{cov}} = 0.2$. Thus, taking $v_{\text{out}} = -0.06c$ and $\mu = 1.2$, the mass outflow rate for zone 1a is $\dot{M}_{\text{out}} = 1 \times 10^{26} \text{ g s}^{-1}$ or $\sim 1.4 M_{\odot} \text{ yr}^{-1}$.

In contrast, as discussed in Section 5.3, the higher-ionization zone may be more homogeneous (and less dense), and we thus estimate the mass outflow rate from Equation (6). Taking $N_{\text{H}} = 10^{22} \text{ cm}^{-2}$, $R \sim 10^{18} \text{ cm}$ from above, $v_{\text{out}} = -0.06c$, and $f_{\text{cov}} = 0.45$, as derived from the emission (see Table 4), $\dot{M}_{\text{out}} = 2 \times 10^{26} \text{ g s}^{-1}$ or $\sim 3 M_{\odot} \text{ yr}^{-1}$. Note that if the assumption of a homogeneous high-ionization absorber is relaxed, as per the variable column density case, where the gas is more dense and closer in (Section 5.2), then $R \sim 10^{17} \text{ cm}$, $n_e \sim 3 \times 10^8 \text{ cm}^{-3}$, and $\Delta R/R \sim 10^{-3}$ for the absorber size scale. In this case, the mass outflow rate from Equation (5) is similar to that obtained for zone 1a, with $\dot{M}_{\text{out}} = 6 \times 10^{25} \text{ g s}^{-1}$ or $\sim 1 M_{\odot} \text{ yr}^{-1}$.

Although these should only be treated as order-of-magnitude calculations, even the more conservative estimate above suggests that the combined mass outflow rate for the soft X-ray absorbers could still be as high as $\sim 2 M_{\odot} \text{ yr}^{-1}$. This is similar to what was calculated by Pounds & Reeves (2009) for

the highly ionized Fe K absorber, $3.4M_{\odot} \text{ yr}^{-1}$, assuming a global covering factor of $f_{\text{cov}} \sim 0.4$, as deduced from the broad ionized emission lines present in the archival *XMM-Newton* spectra. The mass outflow rate either in the soft X-ray band or at Fe K is also similar to the expected Eddington mass accretion rate of PG 1211+143. For a black hole mass of $10^8 M_{\odot}$ and an efficiency of $\eta = 0.1$, $\dot{M}_{\text{Edd}} = L_{\text{Edd}}/\eta c^2 \sim 2M_{\odot} \text{ yr}^{-1}$. Furthermore, the outflow momentum rate is $\dot{M}v \sim L_{\text{Edd}}/c$, which suggests that continuum radiative driving can be important in initially accelerating the gas (King & Pounds 2003). The higher opacity of the soft X-ray absorber compared to that at Fe K may then provide a further boost to the gas acceleration via an enhanced force multiplier factor.

Note that for a total mass outflow rate of $\sim 2 M_{\odot} \text{ yr}^{-1}$ and $v_{\text{out}} = -0.06c$, the total kinetic power of the soft X-ray outflow is $\dot{E}_{\text{K}} = 3 \times 10^{44} \text{ erg s}^{-1}$. This is around 3% of the Eddington luminosity of PG 1211+143; thus, the outflow may be energetically significant in terms of galactic feedback (Hopkins & Elvis 2010). In this regard, PG 1211+143 may be similar to other luminous nearby quasars, such as PDS 456 (Nardini et al. 2015), IRAS F11119+3257 (Tombesi et al. 2015), and Mrk 231 (Feruglio et al. 2015), and may give a view of the feedback processes that are likely to be common in the early universe.

An interesting possibility is that the most highly ionized phase of the outflow, seen in the form of the blueshifted He and H-like Fe K absorption lines in the EPIC-pn spectra (Pounds et al. 2003; Pounds & Reeves 2009; Pounds et al. 2016a), represents the innermost part of the same outflow, launched from a few 100 gravitational radii from the black hole, with the soft X-ray wind observed from further out. This may be the case if the wind follows a shallower radial profile than $n \propto r^{-2}$, with the ionization then decreasing along the flow (Behar 2009; Tombesi et al. 2013). Support for this comes from the similar velocity seen at Fe K in the 2014 EPIC-pn data (Pounds et al. 2016a), where the dominant component of the Fe K outflow has a velocity of $v_{\text{out}} = -0.066 \pm 0.003c$, largely consistent with the main components of absorption seen in the soft X-ray band.

Nonetheless, the existence in the soft X-ray band of two distinct ionization phases suggests that we may be viewing a highly inhomogeneous flow. Indeed, hydrodynamical disk-wind simulations suggest that the outflows are clumpy and also likely to be highly time-variable (Proga et al. 2000; Proga & Kallman 2004; Sim et al. 2010), with the wind perhaps fed by relatively short-lived disk-ejection events (C. Nixon et al. 2018, in preparation). In addition, the presence of denser clumps within the wind, as seen here in the form of low-ionization soft X-ray absorbing gas, could play a role in helping to accelerate the fast wind through the extra boost in line-driving opacity it subsequently provides (Waters et al. 2017) and potentially further still if the gas is of relatively high metallicity.

6. Conclusions

We have presented an in-depth analysis of the high-resolution soft X-ray spectrum of PG 1211+143 taken with the *XMM-Newton* RGS over a baseline of a month in 2014 June. This revealed a rich, soft X-ray spectrum with series absorption lines from He and H-like ions of N, O, and Ne, as well as from L-shell Fe, systematically blueshifted by $-0.06c$ and confirming the earlier analysis by Pounds et al. (2016b). Absorption from lower-ionization gas is also present in the

form of the Fe M-shell UTA, which also appears blueshifted by $-0.06c$. The absorption features can be fitted to an absorber with two distinct ionization states, from low- and high-ionization gas, outflowing at $-0.062 \pm 0.001c$ and $-0.059 \pm 0.002c$, respectively.

These absorption zones were found to be significantly variable on timescales of just days. The column density was found to vary by more than an order of magnitude, driven by the changes in the Fe M-shell UTA, with the overall opacity inversely proportional to the continuum flux. The absorber variations may be explained in the context of a two-phase medium, whereby the variability of the low-ionization gas may be explained by compact clumps (of size scale $\Delta R \sim 10R_g$) passing across our line of sight, while the less dense high-ionization gas may respond to the continuum in terms of its ionization state. The timescales of the variations suggest that the soft X-ray absorbers may be located at a typical distance from the black hole of $R \sim 10^{17} - 10^{18} \text{ cm}$. Overall, the observations imply that the outflow in PG 1211+143 is not a simple homogeneous wind. Future calorimeter observations, such as with *XARM* and *Athena*, will be able to further reveal the structure of the wind in PG 1211+143 at high resolution simultaneously from the soft X-rays up to Fe K.

We would like to thank Valentina Braitto for providing feedback on the paper. J.N. Reeves acknowledges financial support through NASA grant numbers NNX15AF12G, NNX17AC38G, and NNX17AD56G. A. Lobban acknowledges support from STFC via the consolidated grant ST/K001000/1. Based on observations obtained with *XMM-Newton*, an ESA science mission with instruments and contributions directly funded by ESA Member States and NASA.

ORCID iDs

J. N. Reeves  <https://orcid.org/0000-0003-3221-6765>

References

- Arnaud, K. A. 1996, in ASP Conf. Ser. 101, *Astronomical Data Analysis Software and Systems V*, ed. G. H. Jacoby & J. Barnes (San Francisco, CA: ASP), 17
- Behar, E. 2009, *ApJ*, 703, 1346
- Behar, E., Sako, M., & Kahn, S. M. 2001, *ApJ*, 563, 497
- Blustin, A. J., Kriss, G. A., Holczer, T., et al. 2007, *A&A*, 466, 107
- Blustin, A. J., Page, M. J., Fuerst, S. V., Branduardi-Raymont, G., & Ashton, C. E. 2005, *A&A*, 431, 111
- Boroson, T. A., & Green, R. F. 1992, *ApJS*, 80, 109
- Chartas, G., Brandt, W. N., Gallagher, S. C., & Garmire, G. P. 2002, *ApJ*, 579, 169
- Costantini, E., Kaastra, J. S., Arav, N., et al. 2007, *A&A*, 461, 121
- Crenshaw, M. D., Kraemer, S. B., & George, I. M. 2003, *ARA&A*, 41, 117
- Danehar, A., Nowak, M., Lee, J. C., et al. 2018, *ApJ*, in press (arXiv:1712.07118)
- den Herder, J. W., Brinkman, A. C., Kahn, S., et al. 2001, *A&A*, 365, 7
- Detmers, R. G. 2011, *A&A*, 534, A38
- Ferrarese, L., & Merritt, D. 2000, *ApJ*, 539, 9
- Feruglio, C., Fiore, F., Carniani, S., et al. 2015, *A&A*, 583, 99
- Gebhardt, K. 2000, *ApJ*, 539, 13
- Gehrels, N., Chincarini, E., Giommi, P., et al. 2004, *ApJ*, 611, 1005
- Gofford, J., Reeves, J. N., Tombesi, F., et al. 2013, *MNRAS*, 430, 60
- Grevesse, N., & Sauval, A. J. 1998, *SSRv*, 85, 161
- Gupta, A., Mathur, S., & Krongold, Y. 2015, *ApJ*, 798, 4
- Gupta, A., Mathur, S., Krongold, Y., & Nicastro, F. 2013, *ApJ*, 772, 66
- Halpern, J. P. 1984, *ApJ*, 281, 90
- Holczer, T., & Behar, E. 2012, *ApJ*, 747, 71
- Hopkins, P. F., & Elvis, M. 2010, *MNRAS*, 401, 7

- Jansen, F., Lumb, D., Altieri, B., et al. 2001, *A&A*, **365**, 1
- Kaastra, J. S., Mewe, R., Liedahl, D. A., Komossa, S., & Brinkman, A. C. 2000, *A&A*, **354**, L83
- Kaastra, J. S., Steenbrugge, K. C., Raassen, A. J. J., et al. 2002, *A&A*, **386**, 427
- Kalberla, P. M. W., Burton, W. B., Hartmann, D., et al. 2005, *A&A*, **440**, 775
- Kallman, T., Liedahl, D., Osterheld, A., Goldstein, W., & Kahn, S. 1996, *ApJ*, **465**, 994
- Kaspi, S., & Behar, E. 2006, *ApJ*, **636**, 674
- Kaspi, S., Brandt, W. N., George, I. M., et al. 2002, *ApJ*, **574**, 643
- Kaspi, S., Netzer, H., Chelouche, D., et al. 2004, *ApJ*, **611**, 68
- Kaspi, S., Smith, S., Netzer, H., et al. 2000, *ApJ*, **533**, 631
- King, A. R. 2003, *ApJL*, **596**, L27
- King, A. R. 2010, *MNRAS*, **402**, 1516
- King, A. R., & Pounds, K. A. 2003, *MNRAS*, **345**, 657
- Kriss, G. A., Lee, J. C., Danekhar, A., et al. 2018, *ApJ*, in press (arXiv:1712.08850)
- Krongold, Y., Nicastro, F., Brickhouse, N. S., et al. 2003, *ApJ*, **597**, 832
- Lee, J. C., Ogle, P. M., Canizares, C. R., et al. 2001, *ApJ*, **554**, 13
- Lobban, A. P., Pounds, K., Vaughan, S., & Reeves, J. N. 2016a, *MNRAS*, **457**, 38
- Lobban, A. P., Pounds, K., Vaughan, S., & Reeves, J. N. 2016b, *ApJ*, **831**, 201
- Lobban, A. P., Vaughan, S., Pounds, K. A., & Reeves, J. N. 2018, *MNRAS*, in press (arXiv:1801.03858)
- Longinotti, A. L., Costantini, E., Petrucci, P. O., et al. 2010, *A&A*, **510**, 92
- Longinotti, A. L., Krongold, Y., Guainazzi, M., et al. 2015, *ApJ*, **813**, 39
- Marziani, P., Sulentic, J. W., Dultzin-Hacyan, D., Calvani, M., & Moles, M. 1996, *ApJS*, **104**, 37
- McKernan, B., Yaqoob, T., & Reynolds, C. S. 2007, *MNRAS*, **379**, 1359
- Nahar, S. N., & Pradhan, A. K. 2003, *ApJS*, **149**, 329
- Nardini, E., Reeves, J. N., Gofford, J., et al. 2015, *Sci*, **347**, 860
- Netzer, H., Kaspi, S., Behar, E., et al. 2003, *ApJ*, **599**, 933
- Parker, M. L., Pinto, C., Fabian, A. C., et al. 2017, *Natur*, **543**, 83
- Parker, M. L., Reeves, J. N., Matzeu, G. A., Buisson, D. J. K., & Fabian, A. C. 2018, *MNRAS*, **474**, 108
- Peterson, B., Ferrarese, L., Gilbert, K. M., et al. 2004, *ApJ*, **613**, 682
- Pinto, C., Alston, W., Parker, M. L., et al. 2017b, *MNRAS*, submitted (arXiv:1708.09422)
- Pinto, C., Alston, W., Soria, R., et al. 2017c, *MNRAS*, **468**, 2865
- Pinto, C., Fabian, A., Middleton, M., & Walton, D. 2017a, *AN*, **338**, 234
- Pinto, C., Middleton, M. J., & Fabian, A. C. 2016, *Natur*, **533**, 64
- Pounds, K., Reeves, J., O'Brien, P., et al. 2001, *ApJ*, **559**, 181
- Pounds, K. A. 2014a, *MNRAS*, **437**, 3221
- Pounds, K. A. 2014b, *SSRv*, **183**, 339
- Pounds, K. A., & King, A. R. 2013, *MNRAS*, **433**, 1369
- Pounds, K. A., Lobban, A., Reeves, J. N., & Vaughan, S. 2016a, *MNRAS*, **337**, 518
- Pounds, K. A., Lobban, A., Reeves, J. N., Vaughan, S., & Costa, M. 2016b, *MNRAS*, **459**, 4389
- Pounds, K. A., & Page, K. L. 2006, *MNRAS*, **372**, 1275
- Pounds, K. A., & Reeves, J. N. 2007, *MNRAS*, **374**, 823
- Pounds, K. A., & Reeves, J. N. 2009, *MNRAS*, **397**, 249
- Pounds, K. A., Reeves, J. N., King, A. R., et al. 2003, *MNRAS*, **345**, 705
- Pounds, K. A., Reeves, J. N., King, A. R., & Page, K. L. 2004, *MNRAS*, **350**, 10
- Pounds, K. A., & Vaughan, S. 2011, *MNRAS*, **413**, 1251
- Proga, D., & Kallman, T. R. 2004, *ApJ*, **616**, 688
- Proga, D., Stone, J. M., & Kallman, T. R. 2000, *ApJ*, **543**, 686
- Reeves, J. N., Braitto, V., Nardini, E., et al. 2016, *ApJ*, **824**, 20
- Reeves, J. N., O'Brien, P. T., & Ward, M. J. 2003, *ApJ*, **593**, 65
- Reeves, J. N., Porquet, D., Braitto, V., et al. 2013, *ApJ*, **776**, 99
- Reynolds, C. S., & Fabian, A. C. 1995, *MNRAS*, **273**, 1167
- Sako, M., Kahn, S. M., Behar, E., et al. 2001, *A&A*, **365**, 168
- Sim, S. A., Proga, D., Miller, L., Long, K. S., & Turner, T. J. 2010, *MNRAS*, **408**, 1396
- Steenbrugge, K. C., Kaastra, J. S., Crenshaw, D. M., et al. 2005, *A&A*, **434**, 569
- Tarter, C. C., Tucker, W. H., & Salpeter, E. E. 1969, *ApJ*, **156**, 943
- Tombesi, F., Cappi, M., Reeves, J. N., et al. 2010, *A&A*, **521**, 57
- Tombesi, F., Cappi, M., Reeves, J. N., et al. 2011, *ApJ*, **742**, 44
- Tombesi, F., Cappi, M., Reeves, J. N., et al. 2013, *MNRAS*, **430**, 1102
- Tombesi, F., Meléndez, M., Veilleux, S., et al. 2015, *Natur*, **519**, 436
- Turner, A. K., Fabian, A. C., Lee, J. C., & Vaughan, S. 2004, *MNRAS*, **353**, 319
- Verner, D. A., Ferland, G. J., Korista, K. T., & Yakovlev, D. G. 1996, *ApJ*, **465**, 487
- Waters, T., Proga, D., Dannen, R., & Kallman, T. R. 2017, *MNRAS*, **467**, 3160
- Willingale, R., Starling, R. L. C., Beardmore, A. P., Tanvir, N. R., & O'Brien, P. T. 2013, *MNRAS*, **431**, 394
- Wilms, J., Allen, A., & McCray, R. 2000, *ApJ*, **542**, 914